

Key Points:

- We studied the rock magnetism properties of the primitive achondrite Acapulco to pave the way for future paleomagnetic investigations
- While bulk samples are poor recorders, silicate grains with metal inclusions may retain stable magnetizations over 4.5 billion years (Ga)
- The presence of tetraenaite means that Acapulco's parent body was likely not catastrophically disrupted at temperatures $>320^{\circ}\text{C}$

Supporting Information:

Supporting Information may be found in the online version of this article.

Correspondence to:

E. N. Mansbach,
mansbach@mit.edu

Citation:

Mansbach, E. N., Weiss, B. P., Schnepf, N. R., Lima, E. A., Borlina, C. S., Chatterjee, N., et al. (2023). Magnetism of the acapulco primitive achondrite and implications for the evolution of partially differentiated bodies. *Journal of Geophysical Research: Planets*, 128, e2023JE008076. <https://doi.org/10.1029/2023JE008076>

Received 29 AUG 2023

Accepted 17 NOV 2023

Author Contributions:

Conceptualization: Elias N. Mansbach, Benjamin P. Weiss

Data curation: Elias N. Mansbach, Benjamin P. Weiss, Neesha R. Schnepf

Formal analysis: Elias N. Mansbach, Benjamin P. Weiss, Neesha R. Schnepf, Eduardo A. Lima, Cauê S. Borlina

Investigation: Elias N. Mansbach, Benjamin P. Weiss, Neesha R. Schnepf, Nilanjan Chatterjee, Jérôme Gattacceca, Minoru Uehara, Huapei Wang

Methodology: Elias N. Mansbach, Benjamin P. Weiss

© 2023. The Authors.

This is an open access article under the terms of the [Creative Commons Attribution License](https://creativecommons.org/licenses/by/4.0/), which permits use, distribution and reproduction in any medium, provided the original work is properly cited.

Magnetism of the Acapulco Primitive Achondrite and Implications for the Evolution of Partially Differentiated Bodies

Elias N. Mansbach¹ , Benjamin P. Weiss¹ , Neesha R. Schnepf² , Eduardo A. Lima¹ , Cauê S. Borlina^{1,3}, Nilanjan Chatterjee¹ , Jérôme Gattacceca⁴ , Minoru Uehara⁴ , and Huapei Wang⁵ 

¹Department of Earth, Atmosphere, and Planetary Sciences, Massachusetts Institute of Technology, Cambridge, MA, USA, ²Laboratory for Atmospheric and Space Physics, University of Colorado, Boulder, CO, USA, ³Department of Earth and Planetary Science, Johns Hopkins University, Baltimore, MD, USA, ⁴CNRS, Aix Marseille Université, IRD, INRAE, CEREGE, Aix-en-Provence, France, ⁵School of Geophysics and Geomatics, China University of Geosciences, Wuhan, China

Abstract Primitive achondrites like the acapulcoites-lodranites (AL) clan are meteorites that formed on bodies in the process of forming a metallic core, providing a unique window into how early solar system processes transformed unmelted material into differentiated bodies. However, the size and structure of the parent body of ALs and other primitive achondrites are largely unknown. Paleomagnetism can establish the presence or absence of a metallic core by looking for evidence of a dynamo field. We conducted a magnetic study of the Acapulco acapulcoite to determine its ferromagnetic minerals and their recording properties. This is the first detailed rock magnetic and first paleomagnetic study of a primitive achondrite group. We determined that metal inclusions inside silicate grains consist of two magnetic minerals, kamacite and tetraenaite, which have robust recording properties. However, the mechanisms and timing by which these minerals acquired any natural remanent magnetization are unknown. Despite this, Acapulco has not been substantially remagnetized since arriving on Earth and therefore should retain a record dating to 4.55 billion years ago. Future studies could characterize this record by using high-resolution magnetometry measurements of individual populations of grains and developing an understanding of how and when they became magnetized. Our discovery of tetraenaite in ALs provides the first mineralogical evidence for slow cooling [$<5\text{--}10 \times 10^3^{\circ}\text{C}$ per million years (Ma^{-1})] of the AL parent body at low temperatures ($\sim 320^{\circ}\text{C}$). Its presence suggests the AL parent body is unlikely to have been catastrophically disrupted at AL peak temperatures ($\sim 1,200^{\circ}\text{C}$) without subsequent reaccretion.

Plain Language Summary Primitive achondrites are a rare variety of meteorites that formed as the result of limited melting on their parent bodies. They therefore provide key insights into the stages of segregation of metal and rocks in early solar system bodies. However, the sizes and structures of these parent bodies remain uncertain. Here, we conduct a rock magnetic study of the Acapulco acapulcoite to identify the magnetic recorders and to determine if the meteorite could retain a ~ 4.55 billion year old magnetic record. We find that sub-micrometer sized iron-nickel grains embedded in silicate grains should retain a stable magnetization. The presence of high-Ni iron grains suggests acapulcoites cooled slowly at low temperatures, indicating that the parent body could not have been catastrophically disrupted without later reaccretion.

1. Introduction

Meteorites are divided into three classifications. Chondrites are unmelted accretional aggregates of nebular materials, achondrites are melts associated with igneous differentiation on their parent bodies, and primitive achondrites are melt residues from parent bodies that underwent incomplete differentiation (Weisberg et al., 2006). Collectively, they provide records of the thermochemical and geophysical evolution of planetesimals, the <500 km radius rocky-icy parent bodies that served as the building blocks for the planets (Weiss & Elkins-Tanton, 2013). It is typically assumed that many (or perhaps even all) achondrites formed from melting of materials that once formed chondrites. As such, primitive achondrites are of interest because they represent intermediate stages of differentiation and therefore contain unique records of the timescales and mechanisms by which planetary melting processes transformed nebular material into compositionally segregated structures.

Writing – original draft: Elias N.

Mansbach, Benjamin P. Weiss

Writing – review & editing: Elias N.

Mansbach, Benjamin P. Weiss, Neesha

R. Schnepf, Eduardo A. Lima, Cauê S.

Borlina, Nilanjan Chatterjee, Jérôme

Gattacceca, Minoru Uehara, Huapei

Wang

The acapulcoites-lodranites (ALs) are a clan of primitive achondrites composed of two meteorite groups, the acapulcoites and the lodranites. Acapulcoites have bulk near-chondritic compositions that are depleted in Fe-Ni-S melt (<5 vol.% partial melting), average grain diameters of 150–230 μm , and equigranular textures with abundant triple junctions (Keil & McCoy, 2018; McCoy et al., 1996). Acapulcoite mineralogy consists mostly of olivine, pyroxenes, plagioclase, and Fe-Ni-S compounds (Keil & McCoy, 2018; Palme et al., 1981). Some acapulcoites possess mm-to cm-scale metal veins likely representing the initial stages of melt migration on the parent body (Keil & McCoy, 2018; McCoy et al., 1997). They are estimated to have reached peak temperatures of 980–1,170°C during prograde metamorphism (Keil & McCoy, 2018; McCoy et al., 1996), and have metallographic cooling rates 10^3 – $10^5^\circ\text{C Ma}^{-1}$ (million years) from 350 to 600°C (Keil & McCoy, 2018). Lodranites are coarser grained than acapulcoites (average grain diameter 540–700 μm), also depleted in Fe-Ni-S melt, and are sometimes additionally depleted in plagioclase-pyroxene (5–20 vol.% partial melting), indicating that they were heated to higher temperatures (1,150–1,200°C) (Bild & Wasson, 1976; Keil & McCoy, 2018; McCoy et al., 1996). They have metallographic cooling rates on the lower end of the acapulcoite range, generally $10^3^\circ\text{C Ma}^{-1}$ at 350–600°C (Keil & McCoy, 2018). The combination in ALs of a near-chondritic composition largely undepleted in incompatible elements and textural evidence for subsolidus recrystallization with limited melting is the hallmark of a primitive achondrite group. ALs are thought to represent a single, distinct parent body from known meteorites based on their unique oxygen isotope compositions and abundances of volatiles, lithophile, and siderophile elements (Greenwood et al., 2012, 2017; Keil & McCoy, 2018).

The metal in the eponymous acapulcoite Acapulco, which comprises 11.3–22.7 wt.% of the meteorite (Palme et al., 1981; Zipfel et al., 1995), has been reported to occur in two forms: (a) composite 50–500 μm -sized assemblages of kamacite ($\alpha\text{-Fe}_{1-x}\text{Ni}_x$ for $x < 0.06$) and zoned taenite ($\gamma\text{-Fe}_{1-x}\text{Ni}_x$ for $0.06 \leq x \leq 0.5$) located interstitially between silicate grains; and (b) sub- μm to μm -sized kamacite and taenite inclusions in the cores of olivine and pyroxene grains (inclusion average $x = 0.08$), henceforth called metal-bearing silicates (MBSs) (Figure 1) (El Goresy et al., 2005; Keil & McCoy, 2018; Palme et al., 1981; Zipfel et al., 1995). The carriers of any remanent magnetization have not been identified in Acapulco but could possibly be kamacite in interstitial metal assemblages (form 1), inclusions in MBSs (form 2) and/or tetrataenite ($\gamma\text{-Fe}_{0.5}\text{Ni}_{0.5}$) in the high-Ni rims of zoned interstitial taenite (form 1) and MBSs (form 2). Tetrataenite forms from the reordering of taenite at 320°C at cooling rates $< \sim 5,000^\circ\text{C Ma}^{-1}$ (Yang & Goldstein, 2004), which is within the estimated 10^3 – $10^5^\circ\text{C Ma}^{-1}$ metallographic cooling rate range of acapulcoites at 350–600°C (Keil & McCoy, 2018). MBSs are of great interest for possible paleomagnetic studies because they resemble dusty olivine chondrules (DOCs) that have been found to be high-fidelity magnetic recorders in LL and CO chondrites due to their fine metal grain sizes (Borlina et al., 2021; Fu et al., 2014).

Despite the extensive petrological, geochemical, and geochronological analyses of ALs, the size, structure, and thermal history of their parent body remain poorly constrained. Previous thermal modeling suggests that ALs formed in the upper 25 km of a body with a radius of 35–270 km that may have had an Fe-Ni-S core (Golabek et al., 2014; Neumann et al., 2018; Touboul et al., 2009). Differences in cooling rates determined by geochronometers and mineral indicators have led to suggestions the parent body was disrupted while ALs were above $\sim 500^\circ\text{C}$ and then potentially reaccreted (Göpel & Manhès, 2010; Lucas et al., 2022), although an alternate explanation might be the unroofing of overlying material as suggested for IVA irons (Yang et al., 2007). Paleomagnetism can be used to search for evidence of a dynamo magnetic field, which would be direct evidence that the body possessed an advecting, liquid metal core with a diameter of at least several tens of km (Bryson et al., 2019; Weiss et al., 2010). A past dynamo would further suggest that at the time of magnetization acquisition, at least the central portion of the parent body efficiently segregated metal and silicates.

The goal of this study is to address the following questions for Acapulco: (a) Does Acapulco retain a pre-terrestrial natural remanent magnetization (NRM) or has the meteorite been substantially magnetized since falling to Earth?; (b) Does Acapulco retain an interpretable early solar system magnetic record to the present day?; and (c) Can the paleomagnetism and rock magnetic properties of Acapulco constrain the parent body's interior structure and thermal evolution? To answer these questions, we inventory the ferromagnetic mineralogy of the meteorite and constrain its recording properties, its form of NRM [e.g., thermoremanent magnetization (TRM), crystallization remanent magnetization (CRM), and/or shock remanent magnetization (SRM)], and at what temperature that NRM could have been acquired. We address the above questions for both the large interstitial metal grains in bulk samples and the metal inclusions in MBSs. While there has been an initial study of the rock magnetic properties of primitive achondrites (Rochette et al., 2009) and a paleomagnetic study of IAB

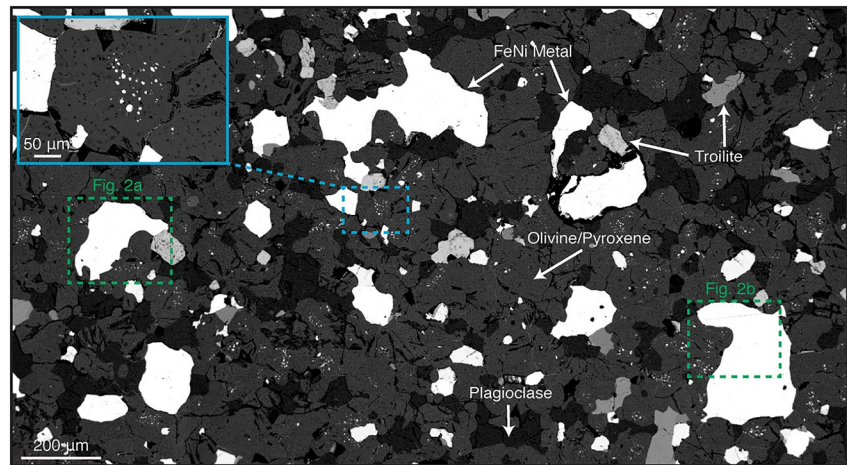


Figure 1. Backscattered electron (BSE) image of Acapulco thin section USNM 5967-1 showing FeNi metal, troilite (FeS), plagioclase, and olivine and pyroxene. The multidomain, interstitial metal grains (50 μm –1 mm in size) dominate the NRM of the bulk samples, making them nonideal magnetic recorders. Blue outlined inset shows a metal-bearing silicate (MBS). Visible in the MBSs are $<10 \mu\text{m}$ FeNi metal grains that may extend into the single domain (SD) or pseudo-single domain (PSD) size range and therefore may have optimal magnetic recording properties. Grains outlined in green dashed boxes are shown in more detail in Figure 2.

iron meteorites (Nichols et al., 2018), which have been proposed to originate from the same parent body as the winonaite primitive achondrite group, no paleomagnetic study has previously been conducted on a primitive achondrite meteorite.

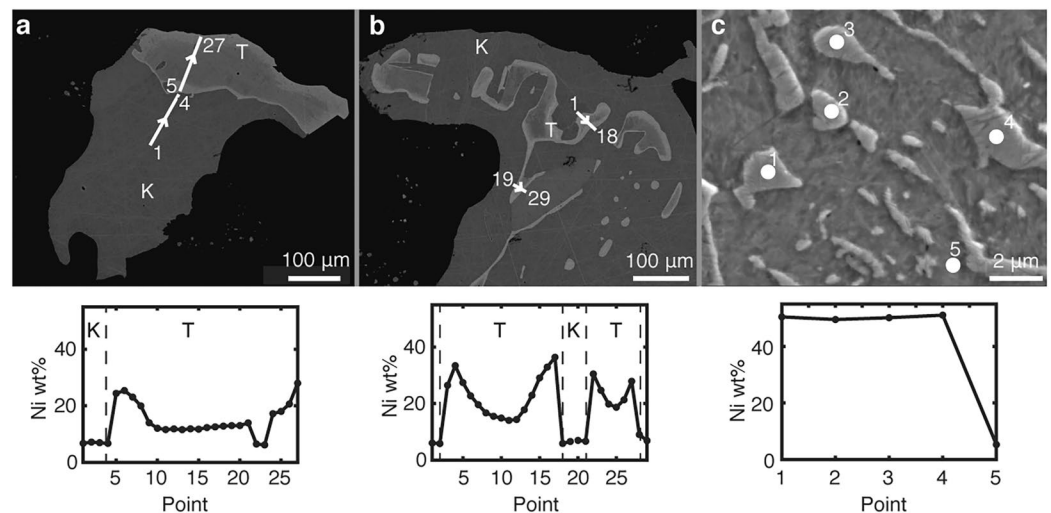


Figure 2. Electron microscopy images and compositions of interstitial metal. (a) BSE image (top) and corresponding WDS measurements (bottom) of an interstitial metal grain (left dashed green box in Figure 1). White line with arrows in the BSE image shows location and direction of the WDS transect. Brightness denotes atomic number, with Fe darker than Ni. These data show that the metal grain is a composite of at least two phases. The bottom section of the grain is uniform in texture and composition with a mean Ni content of 6 wt.%, indicating it is kamacite. The top portion exhibits higher Ni and a zoned composition reaching up to ~ 30 wt.% Ni in the rim and down to ~ 13 wt.% Ni in the center. (b) BSE image of another interstitial metal grain (top) and corresponding WDS transects cover two Ni gradients in a zoned taenite (right dashed green box in Figure 2). The maximum and minimum Ni compositions are 37 and 7 wt.%, respectively. (c) Secondary electron image of plessite in the center of a zoned taenite in an interstitial metal grain (not shown in Figure 1). The precipitates are composed of ~ 50 wt.% Ni, and therefore taenite or tetrataenite, while the matrix is ~ 5 wt.% Ni and therefore kamacite. K = kamacite, T = taenite.

2. Materials and Methods

2.1. The Acapulco Meteorite

We selected Acapulco for analysis because previous studies indicated it may have rock magnetic properties favorable for paleomagnetism. In particular, it is one of only two known AL falls and therefore unlikely to have been weathered on Earth [Acapulco has little to no reported weathering products (Dhaliwal et al., 2017)] or exposed to a hand magnet from a collector (Vervelidou et al., 2023; Weiss et al., 2010). Also, Acapulco retains a fusion crust, which can be used to determine whether the interior of the sample has been remagnetized through a fusion crust baked contact test (see below) (Weiss et al., 2010).

Additionally, Acapulco is essentially unshocked [stage S1 (Palme et al., 1981)]. For the average elongation of kamacite grains in Acapulco (see Text S2 in Supporting Information S1), whose magnetic anisotropy should be dominated by shape, the minimum pressure needed for stress anisotropy to overcome shape anisotropy is 6.4 GPa. For tetrataenite, which is dominated by magnetocrystalline anisotropy, the minimum pressure is 97 GPa (See Text S6 in Supporting Information S1). We also note that analog experiments on FeNi-bearing ordinary chondrites indicate that less than half of a saturating isothermal remanent magnetization (IRM) is lost at pressures up to 1.8 GPa (Bezaeva et al., 2022; Gattacceca et al., 2010). Lastly, we do not observe the presence of Neumann bands, which form from shocks $> \sim 1.5$ GPa (Ohtani et al., 2022), in etched FeNi metal grains in Acapulco. Therefore, it is unlikely that Acapulco was remagnetized or demagnetized through shock.

Furthermore, Acapulco is a promising meteorite for paleomagnetic analysis as $^{40}\text{Ar}/^{39}\text{Ar}$ dating of plagioclase yields ancient ages of $4,554 \pm 43$ Ma (Renne, 2000). For cooling rates between 100 and $100,000^\circ\text{C Ma}^{-1}$, the Ar closure temperature for ~ 100 – 200 μm -sized plagioclase is 300 – 400°C , which is well below the Curie temperature of kamacite (780°C) and spans the ordering temperature of tetrataenite (320°C). Thus, the $^{40}\text{Ar}/^{39}\text{Ar}$ age places a lower bound on the date of any NRM acquisition by kamacite and an upper bound for NRM acquisition by tetrataenite. The ancient $^{40}\text{Ar}/^{39}\text{Ar}$ age also suggests that the samples have not experienced significant metamorphism or impact heating since initial cooling (Palme et al., 1981).

For this study, a 4.02 g piece of Acapulco (USNM 5967) with a fusion crust was provided by the Smithsonian National Museum of Natural History. This sample has a fusion crust on one side that extends < 0.5 mm into the interior. From this main mass, we extracted nine mutually oriented bulk subsamples (masses 5–50 mg), labeled NMMAC1-8 and NMMAC12, containing MBSs and interstitial metal grains. These were cut from the main mass in a transect perpendicular to the fusion crust to sample both the crust and the interior of the sample (Figure S1 in Supporting Information S1). Three subsamples (NMMAC 1, 5, and 12) contained fusion crust and the other six (NMMAC 2–4, and 6–8) sampled the interior at various distances up to a maximum of 7.5 mm from the fusion crust. All samples were photographed and mutually orientated to within 5° uncertainty. In addition to the bulk subsamples, seven MBSs labeled MBS 2–5, 8–10 (masses $\sim 0.12 \pm 0.06$ mg) were extracted from a thick section NMMAC11 (Figures S2 and S3 in Supporting Information S1). The MBSs were also photographed and mutually oriented relative to each other and the bulk samples within 5° uncertainty. We acquired the transect of bulk subsamples from the fusion crust into the interior to determine if the meteorite has been remagnetized after falling to Earth. In particular, because the fusion crust is expected to have acquired a TRM from atmospheric heating, if the meteorite has been remagnetized since landing on Earth (e.g., via a hand magnet, weathering and/or viscous remagnetization in Earth's field), the magnetization directions of the fusion crust and the interior subsamples would be clustered.

In addition to a bulk sample, a $30\text{-}\mu\text{m}$ thin section of Acapulco (USNM 5976-1) was provided by the Smithsonian National Museum of Natural History. The thin section was used primarily to determine the size, texture, habit and composition of the metal grains in Acapulco.

2.2. Compositional and Morphological Methods

We collected backscattered electron (BSE) microscopy images and quantitative compositional measurements of polished MBSs and interstitial metal grains using wavelength dispersive spectroscopy (WDS) on a JEOL JXA-8200 Superprobe electron microprobe machine in the Department of Earth, Atmospheric, and Planetary Sciences at MIT. Following WDS measurements but prior to BSE imaging, the samples were etched with 2% nital for 20 s to enhance grain boundaries associated with metallographic exsolution textures. Additional secondary

electron (SE) images and quantitative compositional measurements using electron dispersive spectroscopy (EDS) were acquired using a Merlin Zeiss Field Emission Gun-SEM in the MIT Material Resources Laboratory. All BSE images and EDS and WDS measurements were conducted on thin section USNM 5967-1. In addition, the morphology and sizes of the metal inclusions in MBSs were determined via transmission X-ray microscope imaging at the National Synchrotron Light Source II (Beamline X8C) at Brookhaven National Laboratory (beam energy 7.2 keV, see Text S2 in Supporting Information S1) (Wang et al., 2015).

2.3. Magnetic Methods

We conducted nearly all magnetic measurements in the Massachusetts Institute of Technology (MIT) Paleomagnetism Laboratory. A 2G Enterprises Superconducting Rock Magnetometer (2G SRM) 755 [2 σ noise floor of 0.99×10^{-12} Am²; Figure S5 in Wang et al. (2017)] equipped with an automatic sample handling and coil system was used for alternating field (AF) demagnetization of bulk and MBS sample NRM. Bulk samples were AF demagnetized up to a maximum of 85 or 145 mT in steps of 0.5–1 mT and their magnetizations were measured using the 2G SRM. The magnetizations were measured after AF application the along *x*, *y*, and *z* axes (ending with *z*) once, and then again after AF application along the *x*, *y*, and *z* axes individually twice. The magnetizations within each AF step were then averaged and rotated from the *x*-*y*-*z* 2G SRM coordinate system into a north-east-up sample coordinate frame (Table S3 in Supporting Information S1).

MBS samples were AF demagnetized to up a maximum field ranging between 500–900 mT in intervals of 10–100 mT. Due to the weak NRMs of the MBSs ($\sim 10^{-11}$ – 10^{-12} Am²), we extracted them from the meteorite (see Text S1 in Supporting Information S1) and their magnetizations were measured using a superconducting quantum interference device (SQUID) microscope (noise floor of 6×10^{-15} Am²), which maps the out-of-the-page (*z*) component of the magnetic field produced by the sample ~ 200 μ m above the MBS (Weiss et al., 2007). The net magnetic moments of MBS samples were determined by performing a dipole fit [dipolarity for the maps were >0.85 (a perfect dipole has a dipolarity of 1) and therefore a multipolar fit was not necessary] to the SQUID microscope maps (Lima & Weiss, 2016). For AF demagnetization up to 145 mT, AF demagnetization was conducted in the *x*, *y*, and *z* directions; following the *z*-application, SQUID microscope maps were made. Such sequences were repeated and the resulting measured moments averaged to reduce spurious anhysteretic remanent magnetization (ARM) (Tikoo et al., 2012). Between 145 and 420 mT, SQUID microscope maps were made after AF demagnetization along each of the three AF axes; these were used to correct for any gyroremanent magnetization acquired during AF demagnetization by averaging the moments measured after each *x*- and *y*-, and *z*-AF application following the Zijderveld-Dunlop method (Stephenson, 1993). Demagnetization above 420 mT was achieved using IRMs applied via a ASC Scientific Model IM-10 impulse magnetometer in alternating directions and decreasing in strength by intervals of 100 mT (i.e., DC demagnetization). Magnetic optical imaging (MOI) was performed at CEREGE in France. Directions of NRM components and their maximum angle of deviation (MAD) values, which provide a measure of angular uncertainty in the components (Khokhlov & Hulot, 2015), were determined by principal component analysis (PCA) (Kirschvink, 1980).

After NRM AF demagnetization, ARMs were applied to bulk samples (130 mT AC field, 200 μ T bias field) and MBSs (145 mT AC field, 200 μ T bias field) to simulate acquisition of a TRM acquired during cooling (Dunlop & Argyle, 1997). AF demagnetizations of these ARMs were compared to those of the NRMs to determine if the NRMs are consistent with a TRM.

The magnetic recording properties of bulk samples and MBSs were assessed through applications and subsequent AF demagnetizations of IRMs on previously demagnetized samples. We used AF demagnetization of a 1 T IRM both to estimate coercivity spectra, which we used to help identify ferromagnetic minerals, and to constrain the origin of NRM overprints through paleointensity estimations. The apparent paleointensity (B_{int}) was calculated as:

$$B_{\text{int}} = \frac{\Delta \text{NRM}}{\Delta \text{IRM}} \cdot a$$

where ΔNRM and ΔIRM are the change in NRM and IRM respectively during AF demagnetization and $a = 3,000$ μ T is an experimentally determined correction factor to account for the ratio of IRM to TRM for kamacite (Gattacceca & Rochette, 2004). We use the term “apparent” here since this estimate assumes a TRM or viscous remanent magnetization (VRM) carried by kamacite; this likely only applies to the low coercivity (<15 mT) fraction of the NRM of the samples.

Thermal demagnetization of IRM was conducted to aid in ferromagnetic mineral identification in MBSs through determination of Curie points. A 1 T IRM was applied to MBSs 5, 8, and 10 and heating was performed using a Magnetic Measurements oven in a controlled atmosphere to limit alteration or creation of new magnetic minerals during heating (Suavet et al., 2014). Consistent with estimates of the oxygen fugacity for Acapulco formation based on olivine-chromite thermometry (Benedix & Lauretta, 2006), we set the oxygen fugacity to -2.3 log units below that of the iron-wüstite (IW) buffer. Heating was conducted in steps of 10 – 50°C up to 770°C with the full heating and cooling time taking 20 min total for each step.

The location and distribution of the magnetic remanence carriers in MBSs were determined using a quantum diamond microscope, which maps the magnetic field with a $\sim 5\text{ }\mu\text{m}$ spatial resolution at a distance of $\sim 10\text{ }\mu\text{m}$ above the sample [moment sensitivity $1 \times 10^{-14}\text{ Am}^2$ (Fu et al., 2020; Glenn et al., 2017)].

To search for the presence of tetrataenite in Acapulco, we conducted first order reversal curve (FORC) measurements on an interior unheated bulk sample and on an interior bulk sample previously heated to 600°C for 20 min. Heating above the ordering temperature of tetrataenite results in disordering of the mineral at a rate that increases with temperature (Dos Santos et al., 2015). In particular, at 600°C , tetrataenite is expected to disorder after <5 min (Dos Santos et al., 2015). The loss of tetrataenite should therefore result in the loss of a high-coercivity phase in the FORC diagram as observed in ordinary chondrites (Gattacceca et al., 2014). The FORCs were measured using a vibrating sample magnetometer in the MIT Department of Material Sciences and Engineering. A total of 83 minor loops were measured, varying the field from -0.66 to 1 T in 20 mT steps. The FORC distribution was determined by taking the mixed second derivative of the magnetization curves in H_A – H_B space [H_A is the starting field of each minor loop and H_B is each field step; see Muxworthy and Roberts (2007)]. The FORC diagrams were created using the FORCinel program (Harrison & Feinberg, 2008) with correction and smoothing parameters provided in Text S3 in Supporting Information S1.

3. Results

To address the three questions in Section 1, we conducted electron, optical, transmission X-ray and magnetic microscopy and compositional analyses of the metal in Acapulco, analyzed the magnetic properties of the metal, and studied the NRM of bulk samples and individual MBSs. These three investigations allow us to determine the ferromagnetic mineralogy, the recording properties of the minerals, and whether Acapulco has been magnetized since falling to Earth.

3.1. Microscopy and Compositional Analysis of Acapulco Metal

We found that interstitial metal grains range in size from $50\text{ }\mu\text{m}$ to 1 mm (Figure 1). Our BSE images and WDS transects of thin section USNM 5967-1 show that the interstitial metal grains consist of two phases: (a) kamacite (5 – $6\text{ wt.}\%$ Ni) and (b) zoned taenite exhibiting Ni gradients from $13\text{ wt.}\%$ near the center of the grains to $37\text{ wt.}\%$ near the rim (Figures 2a and 2b). The zoning is consistent with the “M” shaped profile seen in iron meteorites that forms during subsolidus cooling due to the slower diffusion of Ni through taenite compared to kamacite (Yang & Goldstein, 2005). We did not observe any cloudy zone microstructures in BSE images of the thin section down to $\sim 20\text{ nm}$ resolution after nital etching or in magneto-optical images (Figures S5, S6 in Supporting Information S1).

BSE images of the center of zoned taenite interstitial metal grains show the presence of plessite, a metallic micro- and/or nanostructure that forms from the subsolidus decomposition of martensite ($\alpha_2\text{-FeNi}$) into high- and low-Ni phases [Figure 2c, (Goldstein & Michael, 2006)]. EDS spot measurements of the μm -sized high-Ni precipitates show that their Ni contents reach up to $\sim 50\text{ wt.}\%$ and therefore should be in the form of either taenite or tetrataenite.

Transmission X-ray microscopy shows that unlike the $>50\text{ }\mu\text{m}$ interstitial metal grains, MBSs possess inclusions with sizes <0.4 – $13\text{ }\mu\text{m}$ (Figure S4 in Supporting Information S1). BSE images show that MBS metal grains consist of two types: (type I) a low-Ni FeNi metal phase with some grains possessing a $<1\text{ }\mu\text{m}$, high-Ni rim (Figures 3a and 3b), and (type II) an intergrowth of high-Ni precipitates in a low-Ni matrix (Figures 3b and 3c). Our WDS measurements of type I grains (Figure 3b) show that the low-Ni phase is kamacite ($<6\text{ wt.}\%$ Ni) and that the high-Ni rim, which can reach up to $\sim 50\text{ wt.}\%$, is either taenite or tetrataenite. No Ni compositional gradient is observed in these grains.

Type II metal grains exhibit a plessitic microstructure similar to that observed in the interstitial metal grains, although on a smaller scale (generally sub- μm precipitates compared to the μm -sized precipitates in the interstitial

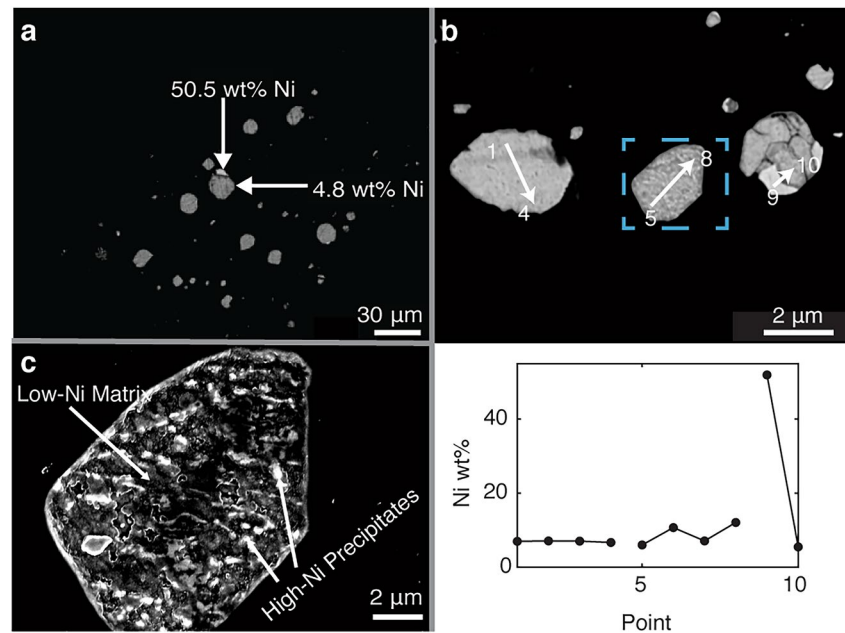


Figure 3. Microscopy images and compositions of MBS metal. (a) BSE image of metal inclusions in an MBS. Most inclusions have apparently homogenous Ni abundances in the range of kamacite with occasional inclusions (<1% of total area) possessing brighter, high-Ni rims [type I grains]. These grains have not been etched with nital. (b) Top: BSE image of metal inclusions in a separate MBS from (a) showing two type I grains on the far left and right and a type II grain in the center. The grains have been etched with nital. Dashed blue box shows location of zoomed BSE image in (c). Bottom: WDS compositions at the locations marked in the BSE image. (c) Zoomed BSE image of the boxed metal inclusion in (b) showing a plessitic microstructure.

metal). Although the small sizes of the precipitates prohibit determination of their composition by EDS and WDS, it is likely that as for plessite in the interstitial grains, some metal grains in the MBS plessite have compositions reaching ~50 wt.% Ni given that such a Ni-rich composition is a natural outcome of plessite formation during slow cooling (Goldstein & Michael, 2006).

3.2. NRM Demagnetization

We analyzed the NRMs of nine mutually oriented bulk subsamples (5–50 mg) of fusion-crust specimen USNM 5967 (labeled NMMAC1–8, 12; Figure S1 in Supporting Information S1) in a transect from the exterior to the interior. Our AF demagnetization revealed that three fusion-crust samples each possessed a common low coercivity (LC) component, denoted LCf, that unblocked between 0 and 3–14 mT depending on the sample (Figures 4a and 4c; Figure S11 in Supporting Information S1). Similarly, all interior bulk samples had a common LC component, denoted LCI, that unblocked between 0 and 5–15 mT (Figures 4b and 4d; Figure S11 in Supporting Information S1). While all bulk samples had a LCI or LCf component, the high average MAD values of 16.8° for these components indicate large directional scatter during demagnetization over the component AF ranges. None of the LCf or LCI components for the fusion-crust or interior samples have a deviation angle (DANG) less than their MAD value (Tauxe & Staudigel, 2004), suggesting they are not origin-trending and therefore not primary components (Table S3 in Supporting Information S1).

The average directions of the LCI and LCf components are 58.8° apart and do not fall within each other's 95% confidence circles (Figure 4e). Because the LCI and LCf α_{95} ellipses overlap, we conducted a common mean bootstrap test (Tauxe, 2010) to determine if the groups of LCI and LCf components share average directions. The two distributions failed the test, indicating that their mean directions are statistically distinct to 95% confidence. Out of the nine samples, we estimated paleointensities for six samples. The paleointensities of the LCf components for the fusion-crust samples NMMAC1 and NMMAC12 are 82.1 ± 15.7 μ T (uncertainties here and elsewhere are 95% confidence intervals) and 79.9 ± 20.3 μ T, respectively, assuming that the LC components are carrying a VRM or TRM. The average paleointensity of the four LCI components calculated for interior samples NMMAC2, NMMAC3, NMMAC7, and NMMAC8 is 42.2 ± 23.1 μ T (Table S3 in Supporting Information S1).

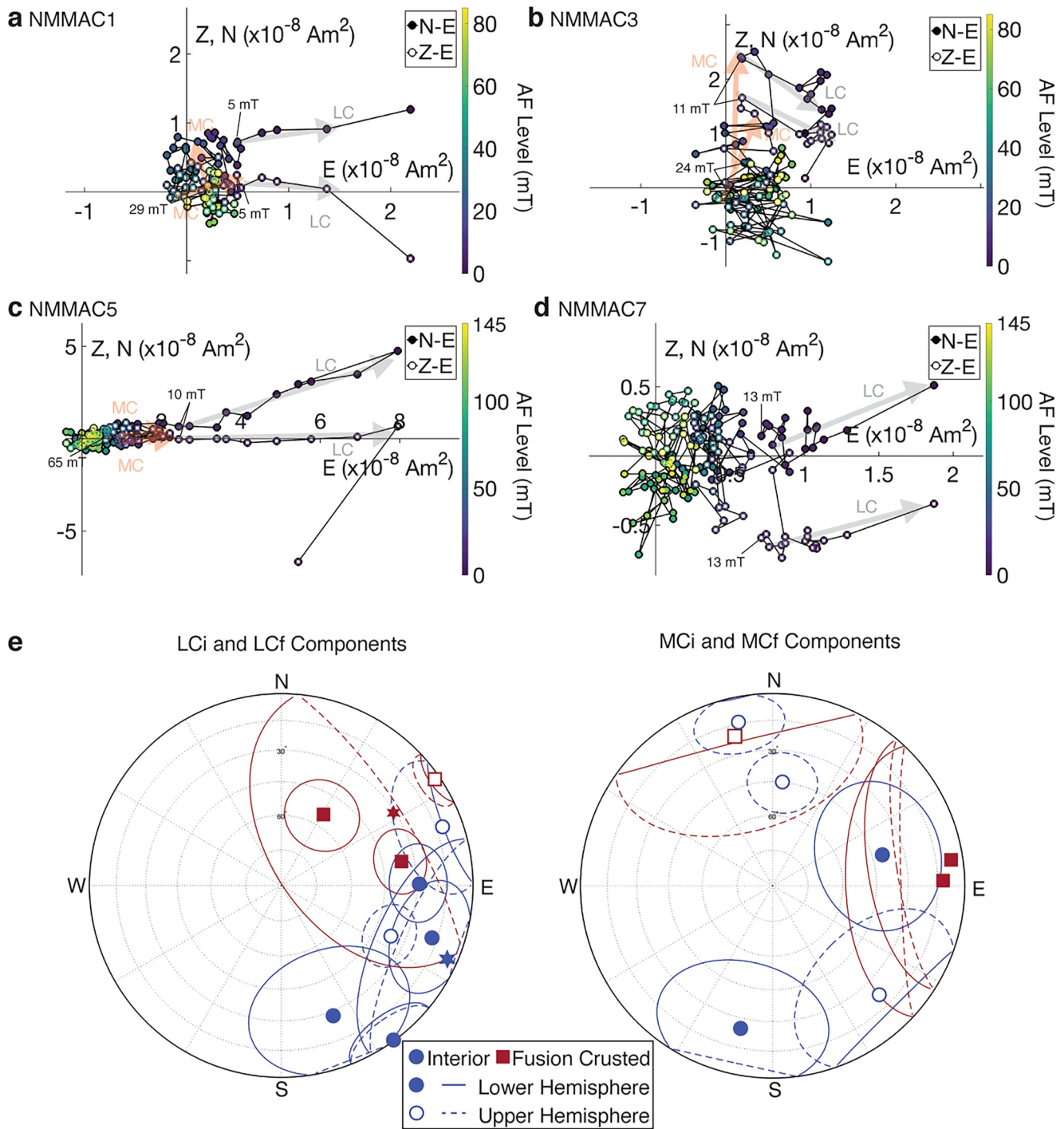


Figure 4. AF demagnetization of bulk sample NRM vectors measured with the 2G SRM. (a)–(d) Orthographic projections of endpoints of NRM vectors onto the north-east (N–E) and up-east (Z–E) planes. LCI/LCf components are denoted by the gray arrows and MCI/MCf components are denoted by the orange arrows. (a) Fusion-crusted sample NMMAC1: an LCf component unblocked between 0 and 4.5 mT and an MC component unblocked between 5.5 and 29 mT. (b) Interior sample NMMAC3: an LCI component unblocked between 0 and 10 mT and an MC component unblocked between 11 and 24.5 mT. (c) Fusion-crusted sample NMMAC5: An LCf component unblocked between 0 and 14 mT and an MC component unblocked between 14.5 and 66 mT. (d) Interior sample NMMAC7: an LCI component unblocked between 0 and 13 mT. Color bars in (a)–(d) denote AF level for each step. (e) Equal area stereographic projection showing LCI/LCf (left) and MCI/MCf (right) component directions for the bulk samples. Fusion-crusted samples are denoted as red squares and interior samples as blue circles. The average fusion-crusted LC direction (red star) and average interior sample LC direction (blue star) fall outside each other's 95% confidence circles, but their confidence circles overlap.

We found that seven of the nine bulk samples possessed a medium coercivity component (denoted MCi for interior samples and MCf for fusion-crust samples) that unblocked starting from the end to the LCi/LCf component to 10–66 mT depending on the sample. After removal of the MCf and MCi components, there were no further identifiable trending components in any sample. We note that no effects were seen from gyroremanent magnetization at large demagnetization fields for any sample [e.g., (Garrick-Bethell et al., 2009)].

Unlike the LCi and LCf components, the individual MCi and MCf component directions are not well-clustered (Figure 4e). Two of the fusion-crust samples (NMMAC5 and 12) show similar (9° difference) MCf component directions, but the direction of the third fusion-crust MCf differs by 106°. The average MAD of the MCi and MCf components is 31.9°, highlighting the scatter in the demagnetization of the samples despite noticeable magnetization trends. The MCf components of bulk samples NMMAC1, 5, and 12, and the MCi component of bulk sample NMMAC6 have $DANG < MAD$, suggesting they may be origin-trending (Table S3 in Supporting Information S1). However, the MAD values of these components are $>30^\circ$, and therefore the components are unlikely to be a primary magnetic record.

AF demagnetization of the NRM of five MBSs did not reveal any clear components, although MBS3 and MBS9 may possess a weak LC component (Figures 5a–5c; S12). The moments of each sample did not exhibit consistent decreases in intensity. Instead, they were clustered (Figure 5b) and/or inconsistently jumped in direction with each AF step (Figure 5c). Similar to the bulk samples, no effects were seen from gyroremanent magnetization. The NRM directions of the MBSs prior to AF demagnetization (Figure 5d) are scattered and not consistent with the LCi or LCf directions.

3.3. Magnetic Properties

AF demagnetization of a saturating 1 T IRM applied to two fusion-crust samples, NMMAC1 and NMMAC12, and two interior samples, NMMAC6 and NMMAC7, revealed different behaviors (Figure 6a). The fusion-crust samples show a rapid decrease in magnetization at lower AF levels, dropping to 50% of their IRM moment (known as the median destructive field [MDF]) at 9 and 14.5 mT for NMMAC12 and NMMAC1 respectively. Comparatively, the interior samples show a slower rate of decrease in moment with AF level and MDFs of 30 and 47 mT for NMMAC7 and NMMAC6, respectively.

By the 130 mT AF step, the two interior samples still retained 19%–25% of their original IRM while the fusion-crust samples had less than 1% of their IRM, indicating that the interior samples contain a larger fraction of recorders with microcoercivities >130 mT (Figure 6a). This behavior is also seen in the coercivity spectra of the samples (Figure 6b), calculated as the derivative of the curve in Figure 6a with respect to AF level: the fusion-crust samples have a factor of 2 larger rate of magnetization loss per AF level compared to the interior samples. However, both interior and fusion-crust samples only show a peak in their coercivity spectra at low AF levels, suggesting that their magnetizations are carried primarily by lower-coercivity grains.

The AF demagnetization behavior of ARMs also differed for fusion-crust samples (Figure 6c) compared to interior samples (Figure 6d). Fusion-crust samples showed a monotonic decrease in moment until ~ 50 mT, after which the moment fluctuated around a constant value. By comparison, the ARMs for the interior samples (Figure 6d) experienced monotonic decreases in moment until AF levels of 10–30 mT depending on the sample, after which their moments showed no further demagnetization with increasing AF level.

The FORC diagram on unheated interior sample NMMAC6 (Figure 8) revealed the presence of a vertically spread, high coercivity signal extending beyond 700 mT consistent with tetrataenite in the cloudy zone (Blukis et al., 2020). This is somewhat surprising because this microstructure is not observed in our BSE images, perhaps due to their ~ 20 nm SEM resolution. In addition, there is a strong signal consistent with multidomain kamacite and an asymmetry below the horizontal axis that may be due to interactions between the higher-coercivity tetrataenite and the lower-coercivity kamacite in plessite (Gattacceca et al., 2014). After heating interior sample NMMAC7 to 600°C, the high-coercivity signal is replaced by a central ridge extending out to ~ 500 mT (Figure 8), which is consistent with kamacite in DOCs (Lappe et al., 2011) rather than tetrataenite. The loss of the high-coercivity signal after heating to 600°C is consistent with the disordering of tetrataenite as has been observed previously in tetrataenite-bearing ordinary chondrites (Dos Santos et al., 2015; Gattacceca et al., 2014).

Quantum diamond microscopy (Glenn et al., 2017) confirms that the main magnetization carriers of the MBSs are metal inclusions in the grain interiors (Figure S9 in Supporting Information S1). AF demagnetization of a

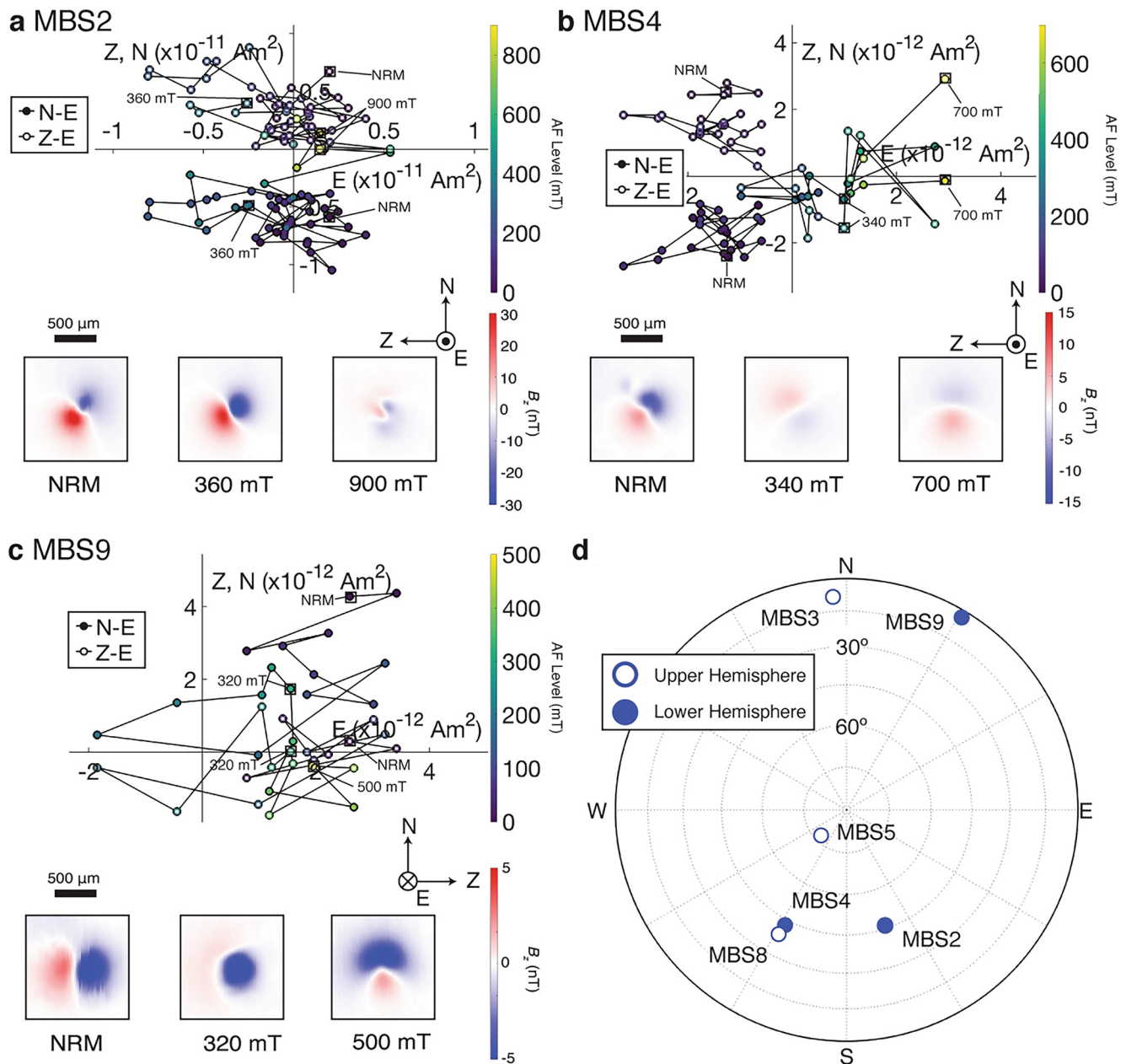


Figure 5. NRM demagnetization of MBSs as measured in the SQUID microscope. (a)–(c) Orthographic projections of endpoints of NRM vectors onto the northeast (N–E) and up-east (Z–E) planes: MBS2 (a) MBS4 (b) and MBS9 (c). Representative SQUID microscope maps at selected field steps for each MBS are shown below and are associated with boxed steps on the orthographic projections. These maps show the vertical component of the magnetic field ~ 0.2 mm above the sample, compasses show orientation of maps. (d) Equal area stereonet showing the NRM direction of MBSs. Open (closed) circles represent NRM directions in the upper (lower) hemisphere of the stereonet.

1 T IRM for MBSs 4, 5, and 8 shows that the silicates retain >22 – 41% of their initial IRM after being demagnetized to 120 mT (Figure 7a). The average MDF of the three MBSs is 65.1 mT, 5.5 and 1.7 times higher than the average MDFs for the fusion-crust bulk samples and interior bulk samples, respectively. Previous AF demagnetizations of 1 T IRMs in DOCs indicate they retain only 8%–24% of their IRM after being demagnetized to 120 mT (Figure 7a). Thus, there is a population of grains in MBSs with microcoercivities exceeding the maximum coercivities observed for DOCs, which are amongst the highest fidelity known magnetic recorders for chondrites (Borlina et al., 2021; Fu et al., 2014; Lappe et al., 2011, 2013). However, the higher rate of loss of magnetization between 0 and 90 mT for MBSs compared to DOCs suggests that MBSs have a larger fraction

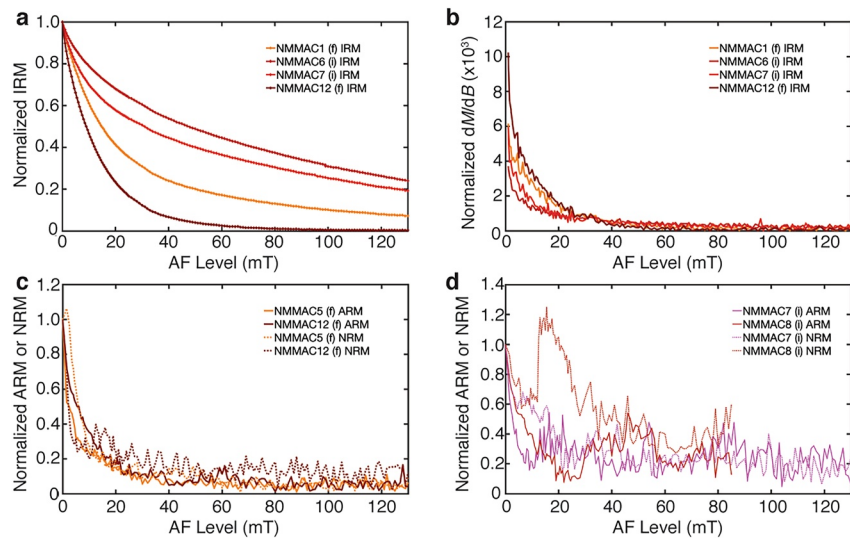


Figure 6. AF demagnetization of IRM and ARM in bulk samples using the 2G SRM. For all figures, (i) and (f) in the legend denote interior and fusion-crusted samples respectively. (a) Normalized IRM demagnetization as a function of AF level. (b) IRM coercivity spectrum calculated by taking the derivative of the data in (a) with respect to AF level. (c) Normalized ARM demagnetization (solid line) and normalized NRM demagnetization (dashed line) vs. AF level for two fusion-crusted samples. (d) Normalized ARM demagnetization (solid line) and normalized NRM demagnetization (dashed line) vs. AF level for two interior samples.

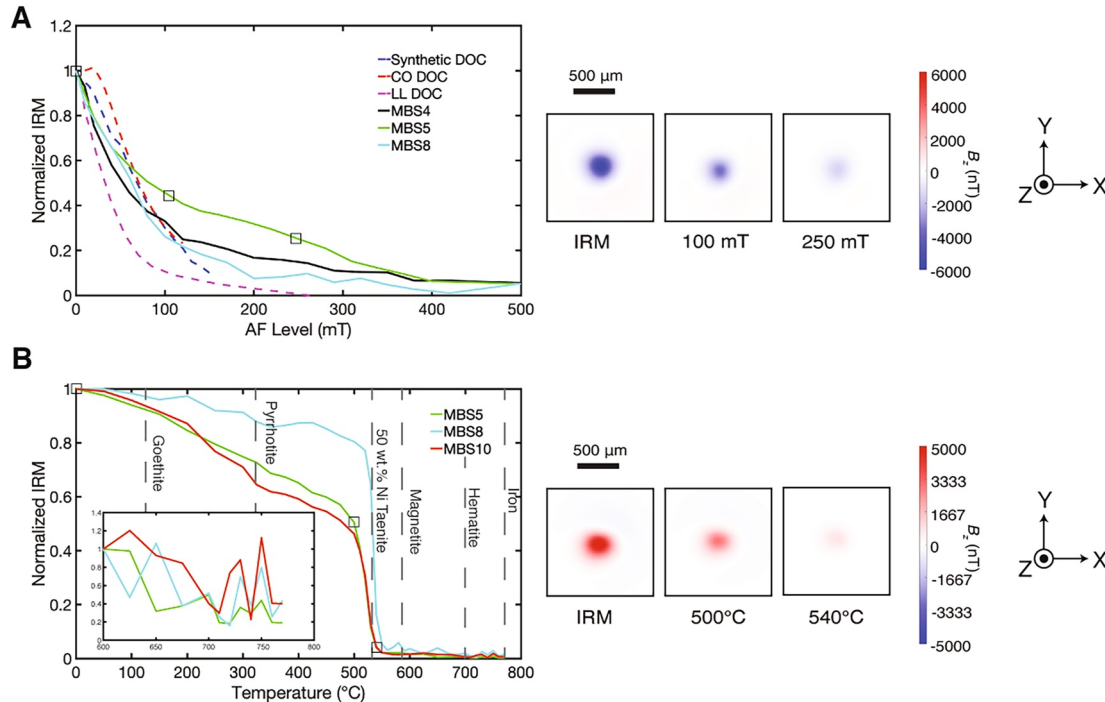


Figure 7. Demagnetization of IRM in MBSs using SQUID microscopy. (a) AF demagnetization of a 1 T IRM for MBSs 4, 5, and 8 compared to a synthetic DOC (Lappe et al., 2011), type 3.00 CO (Dominion Range 08,006) DOC (Borlina et al., 2021), and type 3.00 LL (Semarkona) DOC (Fu et al., 2014). Representative SQUID microscope maps showing the out-of-the-page component of the magnetic field at a height of 200 μm above the sample at selected field steps for MBS 5 are shown. The IRM was applied in the into-the-page ($-z$) direction. (b) Thermal demagnetization of a 1 T IRM for MBSs 5, 8, and 12. The Curie temperatures of various ferromagnetic phases are shown by the dashed gray lines. Representative SQUID microscope maps at selected field steps for MBS 5 are shown. The IRM was applied in the out-of-the-page ($+z$) direction. Inset shows a zoom into the thermal demagnetization from 600 to 770°C. The IRM for each MBS is renormalized to the magnetization at 600°C.

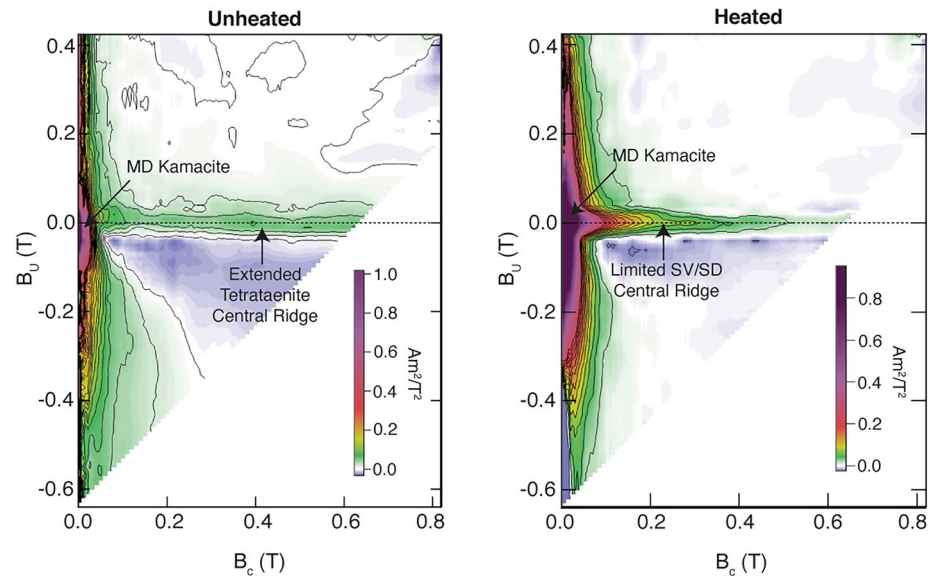


Figure 8. FORC diagrams for unheated bulk interior sample NMMAC6 (left) and bulk interior sample NMMAC7 after heating to 600°C (right). In the unheated sample, a high-coercivity signature is observed that extends beyond 700 mT without evidence for tailing off (tetraetaenite), in addition to a strong multidomain kamacite signal. The asymmetry in the low coercivity region is consistent with interactions between tetraetaenite and low-coercivity phases. After heating, the high-coercivity tetraetaenite signal is lost and transforms into a central ridge that is consistent with kamacite observed in DOCs (Lappe et al., 2011). For ease of viewing, the diagrams are plotted as $B_c = (H_B - H_A)/2$ versus $B_u = (H_B + H_A)/2$.

of metal grains with coercivities below 90 mT, which are very likely the $>1 \mu\text{m}$ metal inclusions visible in BSE images (Figure 1).

Controlled atmosphere thermal demagnetizations of a 1 T IRM applied to three MBSs showed a progressive loss of magnetization in all MBSs during heating from room temperature to 500°C (Figure 7b). The IRM then exhibited a sharp 37%–64% drop between 500 and 540°C, consistent with the Curie temperature of taenite with 49–52 wt.% Ni (Swartzendruber et al., 1991) and/or the loss of IRM from disordering of tetraetaenite by laboratory heating (Dos Santos et al., 2015). We favor the latter explanation given the results from the FORC diagrams above that indicate the presence of tetraetaenite in an unheated bulk sample and subsequent disordering of tetraetaenite after heating to 600°C. Between 600 and 770°C, there is a noisy but noticeable loss in IRM that is likely indicative of kamacite (inset Figure 7b).

4. Discussion and Implications

4.1. Does Acapulco Have a Pre-Terrestrial Magnetic Record?

AF demagnetization of NRM in bulk samples and MBSs and their comparison to laboratory ARMs and IRMs indicate that Acapulco retains a pre-terrestrial magnetic record. We present three lines of evidence supporting this claim: (a) $\text{NRM}/\text{IRM} < 1.5\%$, (b) directional scatter in MC components in bulk samples (i.e., passed Watson randomness test), and (c) lack of terrestrial weathering products.

The low NRM/IRM values ($< 1.5\%$; Tables S1, S2 in Supporting Information S1) of the MBSs and bulk samples suggest that the interior of Acapulco was not substantially remagnetized by an external field since falling to Earth. Since the expected proportion of magnetic recorders aligned with an Earth-strength external field during cooling (TRM efficiency) is $\sim 1\%$ of saturation IRM (McClelland, 1996; Yu et al., 2007), the NRM/IRM of the samples are consistent with a natural form of magnetization and not artificial contamination (e.g., from a hand magnet), which would produce $\text{NRM}/\text{IRM} > 10\%$ (Vervelidou et al., 2023).

The MCi/MCf components of bulk samples are scattered (Figure 4) and the NRM directions of the MBSs vary in direction as well (Figure 5). This is consistent with a lack of a strong overprint which would align the magnetizations of the bulk samples and MBSs. While curved fields around hand magnets can create NRMs with smoothly

varying directions as a function of depth in a sample and multiple exposures to hand magnets of different strengths from different orientations could create a scatter in the magnetization directions (Vervelidou et al., 2023), the low NRM/IRM values preclude this possibility for Acapulco. This is consistent with Acapulco being a fall given that magnet remagnetization mainly affects meteorite finds [e.g., (Weiss et al., 2008)].

Lastly, thermal demagnetizations of IRMs in MBSs show that the remanence carriers are predominantly FeNi metal alloys (Figure 7b). Common terrestrial phases that could form from weathering and oxidation of meteoritic metal include magnetite, hematite, and goethite (Uehara et al., 2012; Weiss et al., 2010). There is no observed drop in magnetization after heating to the Curie temperatures for those minerals.

While the LCf and LCi directions are statistically distinct and therefore Acapulco technically passes the fusion crust baked contact test, the directions' relative proximity could be interpreted as indicating uncertainty as to whether Acapulco actually passes that test. The proximity in the average directions could be due to a VRM acquired by the low-coercivity metal grains while immersed in Earth's magnetic field prior to NRM demagnetization. This interpretation is supported by the LCi/LCf paleointensities that are consistent with an Earth-strength field. Thus, the interior sample LCi directions would retain the VRM while the fusion-crusted LCf directions are an admixture of the VRM and a magnetization acquired during atmospheric entry. We note that the shapes of the fusion-crusted samples' ARM and NRM demagnetization curves are similar (Figure 6c), suggesting that the LCf components in the samples are at least partially a TRM. This is expected since the fusion crust was a melt produced during atmospheric entry that cooled in Earth's magnetic field. In contrast, the ARM and NRM demagnetization curves for the interior samples are different: the ARM demagnetizes monotonically up to 10–20 mT while the NRM moment is noisy and does not decline much in magnitude (Figure 6d). Regardless of the fusion crust baked contact test results, the scatter in the MCi/MCf components indicates that the external field source of the LCi/LCf component did not fully magnetize Acapulco.

4.2. Can Acapulco Reliably Retain an Early Solar System Magnetization?

The two major ferromagnetic recorders in Acapulco are kamacite and tetrataenite. Kamacite is clearly identified by its low-Ni composition. We interpret the high-Ni phases in MBSs and the plessitic microstructures to be tetrataenite rather than taenite on account of their high coercivities (>700 mT), changes in sample coercivity after heating, and Ni composition, in addition to further magnetic measurements discussed in the supplement. For bulk interior samples, Acapulco's NRM, ARM, and IRM are dominated by kamacite in the large interstitial metal grains. While there is evidence from our microscopy and magnetic data that tetrataenite is present in the plessitic cores of zoned taenite grains and MBSs, these precipitates' magnetizations are masked by the larger and more abundant kamacite. Kamacite that forms above its Curie temperature will record a TRM upon cooling. However, the morphology of the kamacite and the observed Ni gradients in the interstitial metal grains provide evidence of formation by subsolidus recrystallization of taenite as Ni is diffused out of the crystal structure. Hence, the kamacite in Acapulco would likely have recorded thermochemical remanent magnetization (TCRM), a form of remanence for which reliable paleointensity estimates have not yet been developed (Garrick-Bethell & Weiss, 2010). Furthermore, the various kamacite grains in the interstitial metal likely passed through their blocking temperatures at different times. If a magnetic field was present in the region where ALs formed, the NRM of the bulk samples would be the sum of magnetizations acquired at different periods in time under potentially different field strengths and orientations. This could lead to scattered MCi/MCf directions. We note that the <1.5 GPa shock state of Acapulco indicates that its NRM is almost certainly not an SRM (see Section 2.1) and that it is unlikely to have been substantially demagnetized or remagnetized by shock pressures or heating since 4.55 Ga (Bezaeva et al., 2022; Weiss et al., 2010).

For MBSs, Acapulco's NRM, IRM, and ARM are carried by kamacite and tetrataenite. Tetrataenite would record a CRM during its formation by the reordering of taenite when the meteorite cooled through 320°C (Einsle et al., 2018). Type I grains in MBSs are either present as pure kamacite or show evidence of subsolidus recrystallization in the form of a high-Ni rim. Thus, these grains either recorded a TRM during cooling or a similar TCRM as the kamacite in the interstitial metal grains in the bulk samples. Type II metal grains, which formed from decomposition of martensite into plessite at temperatures <500°C (Goldstein & Michael, 2006), have kamacite and tetrataenite that would record a TCRM. The TCRM for the kamacite would be recorded at the decomposition temperature and the TCRM for tetrataenite would be recorded at and below 320°C. We note that given the metallographic cooling rates reported for Acapulco [10^3 – 10^5 °C Ma⁻¹ at 350–600°C (Keil

& McCoy, 2018)], the time difference between 780°C and 320°C could be 0.005–0.5 Ma. Therefore, similar to the bulk samples, the NRM of the MBSs are likely aggregates of magnetizations produced at different times and possibly different external field conditions. As with the bulk samples, this could lead to scattered NRM and component directions.

Kamacite and tetrataenite that occupy the single domain (SD) or single vortex (SV) states can retain magnetizations stable against viscous relaxation over solar-system timescales (Mansbach et al., 2022; Shah et al., 2018). Electron holography of kamacite inclusions with a range of elongations in a synthetic DOC shows that grains up to ~250 nm occupy the SD or SV state (Lappe et al., 2013). In Acapulco bulk samples, the >50 μm size of the kamacite in the interstitial metal suggests that they are most likely multidomain and therefore poor magnetic recorders. However, sub- μm kamacite grains in MBSs could occupy the SV or SD state.

Based on micromagnetic modeling results, non-interacting tetrataenite occupies the SD state between 6 and ~160 nm depending on its elongation (Mansbach et al., 2022), though we note that interacting tetrataenite grains in the cloudy zone microstructure have been observed to act as SD grains at sizes <~150 nm even when falling outside the predicted SD stability region (Nichols et al., 2020). Unlike kamacite, tetrataenite does not have an SV state and transitions directly from the SD state to a two-domain state due to its high magnetocrystalline anisotropy (Mansbach et al., 2022). The sizes of the tetrataenite grains in the bulk samples (μm) and MBSs (μm to sub- μm) indicate that they are likely multidomain. However, micromagnetic modeling of two-domain tetrataenite shows that the mineral can retain a stable magnetization against viscous relaxation and external remagnetization over the lifetime of the solar system (Mansbach et al., 2022). Therefore, the tetrataenite grains in Acapulco may hold a NRM dating back to near the time of its formation at 4.55 Ga.

4.3. How Can the Paleomagnetism and Rock Magnetic Properties of Acapulco Constrain the Parent Body's Interior Structure and Thermal Evolution?

The identification of tetrataenite provides a powerful cooling rate constraint on the AL parent body. An additional constraint could be derived from the fact that we do not observe cloudy zones in our BSE images. A limitation with the latter is that, as mentioned above, the islands may be smaller than the resolution of the BSE images (<20 nm) [e.g., like those observed in some IVA irons (Yang et al., 2007)] and therefore additional transmission electron microscope analysis is required to confirm the lack of a cloudy zone. We interpret the presence of tetrataenite and the provisional absence of a cloudy zone as follows. Ordering from taenite to tetrataenite is estimated to occur for maximum cooling rates of ~5,000°C Ma⁻¹ at 320°C (Yang & Goldstein, 2004), while the cloudy zone microstructure forms at an estimated maximum cooling rate of ~10,000°C Ma⁻¹ at 350°C (Maurel et al., 2019). It is currently not clear if the uncertainties on these two critical cooling rates overlap. If they are not within error of each other, this would mean that any meteorite with a high-Ni taenite rim containing tetrataenite should also have formed a cloudy zone in this region. If a cloudy zone is in fact present in Acapulco, then the maximum cooling rate at 350°C is ~5,000°C Ma⁻¹. If no cloudy zone is present, then we would interpret this under the assumption that the two critical cooling rates have overlapping uncertainties, in which case Acapulco cooled <~10,000°C Ma⁻¹ at 320°C. In summary, our data indicate that Acapulco cooled slower than ~5,000–10,000°C Ma⁻¹ at 320–350°C, which is consistent with the reported metallographic cooling rates 10³–10⁵°C Ma⁻¹ at temperatures of 350–600°C for acapulcoites (Keil & McCoy, 2018), albeit on the lower end of that range.

Our reported cooling rate at 320–350°C has important implications for the thermal evolution of the AL parent body. ALs must have been part of a body at least 2 km in radius based on recent cooling rates reported for lodranites (Lucas et al., 2022). For such a 2 km radius body, ALs would have to be located within 10% of the radius of the center of the body. The depth of emplacement within the body decreases as the size of the body increases. Therefore, either the AL parent body was never disrupted prior to cooling through 320°C and instead underwent monotonic cooling through this temperature, or the body was disrupted above this temperature and ALs were later reaccreted into a secondary body of at least a few km in radius. The low-temperature cooling rate constraint imposed by tetrataenite suggests it is highly unlikely that the AL parent body was catastrophically disrupted and did not undergo at least partial recreation.

The presence of two ferromagnetic minerals in Acapulco that would have acquired their NRM at different times enables the possibility of further constraining the thermal evolution of the parent body under the assumption that the two minerals acquire magnetizations independently of each other. Recent discussion of the potential inheritance of NRM during pseudomorphic replacement of FeNi metal to magnetite (Borlina et al., 2022; Bryson et al., 2023) suggests that the influence of kamacite on neighboring taenite and the inheritance of tetrataenite magnetization from the precursor taenite should be studied further. Here, we present the methods by which a future paleomagnetic study of Acapulco or other members of the AL clan could elucidate the structure and history of the body. We consider that the parent body experienced one of four evolutionary paths (Figure 9) after initial heating of the AL source region [outer 7–25 km (Neumann et al., 2018)] (ALSR), to peak temperatures of 1,200°C [note that the deeper interior could have reached 1,625°C as suggested by three-dimensional thermal modeling of the parent body (Neumann et al., 2018)]: 1) Continuous cooling without major disruption by impacts; 2) Catastrophic disruption at the time that the ALSR reached its peak temperature followed by re-accretion and final cooling; 3) Catastrophic disruption when the temperature of the ALSR \sim 500°C and then re-accretion and final cooling; 4) Catastrophic disruption at the time that the ALSR reached its peak temperature followed by no reaccrction.

In each path, we start with the ALSR having reached its peak temperature and possessing an onion-shell structure as suggested by previous thermal models (Golabek et al., 2014; Neumann et al., 2018; Touboul et al., 2009). We allow for a chondritic crust to overlay a primitive achondritic layer that in turn overlies an igneous silicate region and possibly also a metallic core. In Case 1A, we consider a parent body evolution model in which the body possessed a tens of km radius metallic core that was capable of generating a dynamo (Bryson et al., 2019; Dodds et al., 2021; Weiss et al., 2010) on the tens-hundreds of Ma timescale like that found for IIE irons (Maurel et al., 2020, 2021). In this scenario, the ALSR cools continuously from peak temperatures down to below 320°C. If the dynamo was present continuously, then both kamacite and tetrataenite in Acapulco would have acquired a NRM record of the dynamo during cooling through their blocking and ordering temperatures of 780°C (or lower as suggested by subsolidus recrystallization) and 320°C, respectively. However, the external field direction and strength may have changed between the times at which the NRMs were acquired by the two minerals or even changed while each mineral acquired its NRM.

In Case 1B, we consider the scenario in which the parent body continuously cooled, but there was either no core present or a core was present but was not able to generate a dynamo field. In this case, the parent body cools through the ordering and blocking temperatures of tetrataenite and kamacite but there is no external field recorded. In Case 2, the parent body was disrupted around ALSR peak temperatures and then reaccrcted as solid fragments prior to ALSR cooling to 750°C [following (15)]. We expect that it is unlikely that a molten core formed that was sufficiently large to be able to generate a dynamo on the secondary body. Therefore, in both Cases 1B and 2, kamacite and tetrataenite would not have recorded a dynamo field.

In Case 3, the parent body was disrupted at a temperature after the ALSR cooled to below the blocking temperature of kamacite. In Case 3A, the parent body possessed a dynamo and the ALSR cooled through 780°C, which would enable the kamacite to retain a record of the external field. However, the body was then disrupted at ALSR temperatures \sim 500°C [as suggested by ref. (Göpel & Manhès, 2010)], and subsequently reaccrcted. As before, it is highly unlikely that there would have been an advecting metal core capable of creating a dynamo field after reaccrction, and therefore the tetrataenite would not have recorded any field when the ALSR reached 320°C. However, as noted previously, this assumes that the remanence of kamacite has no effect on the magnetization of the tetrataenite. Case 3B describes the evolution of a body that had no dynamo prior to disruption and therefore no dynamo field was recorded by the kamacite or tetrataenite.

In Case 4, the parent body is catastrophically disrupted into pieces <2 km in radius at ALSR peak temperatures and never reaccrcted. As discussed previously, this path is not likely as ALs must have cooled at rates $<\sim 5,000\text{--}10,000^\circ\text{C Ma}^{-1}$ at 320–350°C.

In summary, a thorough understanding of the paleomagnetic record of the tetrataenite and kamacite separately in ALs may distinguish between different parent body evolution paths. In the case where no field is recorded by either kamacite or tetrataenite, we would be unable to differentiate between Cases 1B, 2, or 3B. However, if both tetrataenite and kamacite show evidence for a dynamo field being present at their respective NRM acquisition temperatures, then the parent body was not likely disrupted and followed the path described in

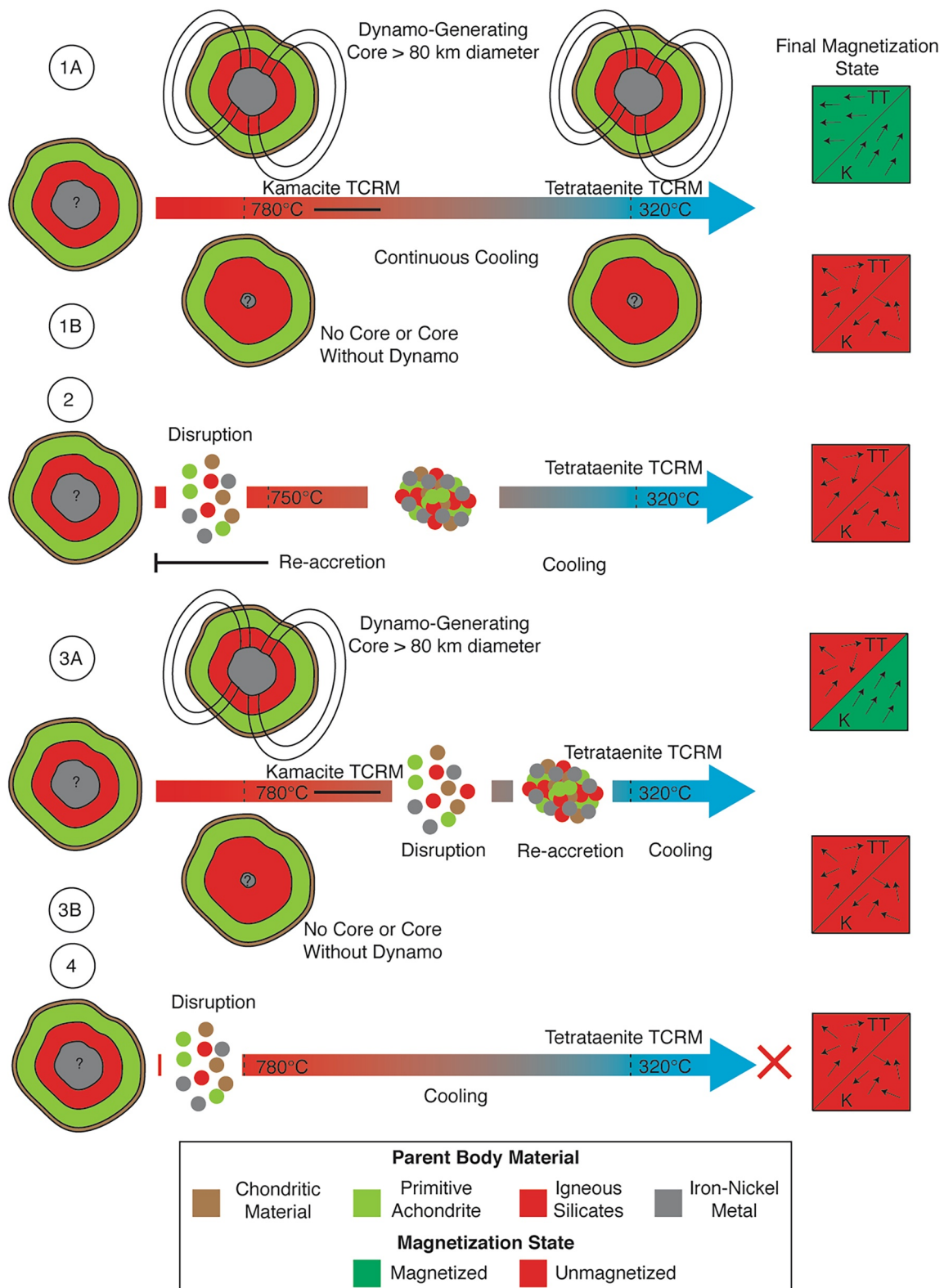


Figure 9.

Case 1A. In this scenario, one potential explanation for the varying cooling rates reported for ALs could be impact unroofing of the material overlaying the ALs. Lastly, if kamacite contains an NRM record of a dynamo, but tetrataenite does not, then this would be consistent with catastrophic disruption below 780°C (i.e., Case 3A). However, an alternate explanation is that the dynamo ceased prior to reaching 320°C on a non-disrupted parent body.

Given the uniquely powerful ability of paleomagnetism to independently confirm the presence or absence of a dynamo on the AL parent body and therefore a metallic core larger than ~80 km in diameter (Weiss et al., 2010), further evaluation of the paleomagnetic record of ALs could provide valuable information to distinguish between the four abovementioned scenarios. Future paleomagnetic studies should focus on MBSs as they contain magnetic recorders that are more likely to be SD or SV compared to the bulk samples. However, an additional understanding of the acquisition of TCRMs by kamacite and tetrataenite is warranted prior to re-evaluating the paleomagnetic record of Acapulco. Alternately, future identification with transmission electron microscopy of a cloudy zone microstructure in Acapulco could enable a paleomagnetic study using X-ray photoemission electron microscopy (Bryson et al., 2014). An additional option for AL paleomagnetic studies is to focus on those ALs with MBSs that cooled at rates $>5,000$ to $10,000^{\circ}\text{C Ma}^{-1}$ and therefore would not possess tetrataenite. As an example, the Monument Draw acapulcoite has a reported metallographic cooling rate of $\sim 10^4^{\circ}\text{C Ma}^{-1}$ over the temperature range 600–350°C (McCoy et al., 1996). No lodranites have reported cooling rates around 320°C that are above $10^4^{\circ}\text{C Ma}^{-1}$ (Keil & McCoy, 2018). However, an alternative path is to identify very slowly cooled lodranites ($<10^3^{\circ}\text{C Ma}^{-1}$) and search for cloudy zones as well.

5. Conclusions

- We present the results of a rock magnetic study of Acapulco and provide the initial results of the first paleomagnetic study of a primitive achondrite to determine if the parent body possessed a planetesimal dynamo.
- The major magnetic phases in bulk Acapulco samples are multidomain kamacite and tetrataenite, though there may be SD tetrataenite present in the plessite.
- The major magnetic phases in MBSs are kamacite and tetrataenite as well, but with smaller, potentially SD or SV grains sizes.
- Acapulco shows no evidence of remagnetization from a magnet or terrestrial weathering and therefore can retain a pre-terrestrial magnetic record.
- Bulk samples are poor recorders due to large interstitial metal grains that dominate the measured NRM magnetization.
- The NRM magnetizations in MBSs are summations of multiple ferromagnetic minerals that would have acquired magnetizations at different times and in different forms, leading to complex NRMs that do not allow us to definitely conclude that a dynamo was present or absent on the parent body.
- No primary NRM components were isolated during AF demagnetization of MBS.
- The presence of tetrataenite indicates that Acapulco underwent slow cooling ($<\sim 5,000$ – $10,000^{\circ}\text{C Ma}^{-1}$) at 320–350°C. This suggests that it is highly unlikely that the parent body was catastrophically disrupted while Acapulco was at peak temperatures without subsequent reaccretion.
- Future paleomagnetic investigations of Acapulco that can interpret the magnetization of kamacite and tetrataenite separately may be able to determine the evolution of the parent body.

Figure 9. Parent body evolution scenarios. In Case 1, the parent body cooled without being disrupted and possessed (Case 1A) or lacked (Case 1B) a dynamo. We note that the direction of the cartoon magnetization is chosen to be arbitrary. In Case 2, the parent body was disrupted by impacts at peak temperatures and subsequently reaccreted to form a secondary body of at least 2 km in radius. No dynamo ever formed in this scenario. In Case 3, the parent body began to cool but was later disrupted and reaccreted. If a dynamo was present prior to disruption (Case 3A), then the kamacite would have acquired NRM in the field. In Case 4, the parent body was catastrophically disrupted at peak temperatures and never reaccreted. The cooling rate threshold imposed by the presence of tetrataenite excludes Case 4 for the AL parent body (as denoted by “X”). The final magnetization states of the kamacite and tetrataenite for each Case are shown to the right. *K* = kamacite, *T* = tetrataenite.

Data Availability Statement

Magnetization files that contain data on the NRM demagnetization of all bulk samples and their magnetic properties used to draw the conclusions in this paper can be found on the Magnetism Information Consortium (MagIC) database via <https://doi.org/10.7288/V4/MAGIC/19872> (Mansbach et al., 2023) as a zip file. The MagIC database DOI also contains .mat files with all SQUID maps taken of MBS magnetizations including NRM demagnetization, thermal demagnetization, ARM demagnetization, and IRM demagnetization.

Acknowledgments

We acknowledge funding from NASA FINESST Grant 80NSSC20K1366 and a private gift from Thomas F. Peterson, Jr. We thank Tim Grove for productive conversations about primitive achondrites and planetary differentiation and Caroline Ross for the use of her vibrating sample magnetometer. We also thank Tim McCoy and the Smithsonian Institution staff for providing meteorite samples for this study. Lastly, we thank Wyn Williams and Richard Harrison for insightful and constructive reviews to improve the manuscript.

References

- Benedix, G. K., & Lauretta, D. S. (2006). Thermodynamic constraints on the formation history of acapulcoites. *Lunar and Planetary Science Conference*, 37, 2129.
- Bezaeva, N. S., Gattacceca, J., Rochette, P., & Sadykov, R. A. (2022). Demagnetization of ordinary chondrites under hydrostatic pressure up to 1.8 GPa. *Geochemistry International*, 60(5), 421–429. <https://doi.org/10.1134/s0016702922050032>
- Bild, R. W., & Wasson, J. T. (1976). The Lodran meteorite and its relationship to the ureilites. *Mineralogical Magazine*, 40(315), 721–735. <https://doi.org/10.1180/minmag.1976.040.315.06>
- Blukis, R., Pfau, B., Günther, C. M., Hessing, P., Eisebitt, S., Einsle, J., & Harrison, R. J. (2020). Nanoscale imaging of high-field magnetic hysteresis in meteoritic metal using X-ray holography. *Geochemistry, Geophysics, Geosystems*, 21(8), e2020GC009044. <https://doi.org/10.1029/2020gc009044>
- Borlina, C. S., Weiss, B. P., Bryson, J. F. J., & Armitage, P. J. (2022). Lifetime of the outer solar system nebula from carbonaceous chondrites. *Journal of Geophysical Research: Planets*, 127(7), e2021JE007139. <https://doi.org/10.1029/2021je007139>
- Borlina, C. S., Weiss, B. P., Bryson, J. F. J., Bai, X., Lima, E. A., Chatterjee, N., & Mansbach, E. N. (2021). Paleomagnetic evidence for a disk substructure in the early solar system. *Science Advances*, 7(42), eabj6928. <https://doi.org/10.1126/sciadv.abj6928>
- Bryson, J. F. J., Herrero-Albillos, J., Kronast, F., Ghidini, M., Redfern, S. A. T., van der Laan, G., & Harrison, R. J. (2014). Nanopaleomagnetism of meteoritic Fe–Ni studied using X-ray photoemission electron microscopy. *Earth and Planetary Science Letters*, 396, 125–133. <https://doi.org/10.1016/j.epsl.2014.04.016>
- Bryson, J. F. J., Neufeld, J. A., & Nimmo, F. (2019). Constraints on asteroid magnetic field evolution and the radii of meteorite parent bodies from thermal modelling. *Earth and Planetary Science Letters*, 521, 68–78. <https://doi.org/10.1016/j.epsl.2019.05.046>
- Bryson, J. F. J., Nichols, C. I. O., & Mac Niocaill, C. (2023). A unified intensity of the magnetic field in the protoplanetary disk from the Winchcombe meteorite. *Meteoritics & Planetary Sciences*. <https://doi.org/10.1111/maps.14079>
- Dhaliwal, J. K., Day, J. M. D., Corder, C. A., Tait, K. T., Marti, K., Assayag, N., et al. (2017). Early metal-silicate differentiation during planetesimal formation revealed by acapulcoite and lodranite meteorites. *Geochimica et Cosmochimica Acta*, 216, 115–140. <https://doi.org/10.1016/j.gca.2017.06.042>
- Dodds, K. H., Bryson, J. F. J., Neufeld, J. A., & Harrison, R. J. (2021). The thermal evolution of planetesimals during accretion and differentiation: Consequences for dynamo generation by thermally-driven convection. *Journal of Geophysical Research: Planets*, 126(3). <https://doi.org/10.1029/2020je006704>
- Dos Santos, E., Gattacceca, J., Rochette, P., Fillion, G., & Scorzelli, R. B. (2015). Kinetics of tetraenaite disordering. *Journal of Magnetism and Magnetic Materials*, 375, 234–241. <https://doi.org/10.1016/j.jmmm.2014.09.051>
- Dunlop, D. J., & Argyle, K. S. (1997). Thermoremanence, anhysteretic remanence and susceptibility of submicron magnetites: Nonlinear field dependence and variation with grain size. *Journal of Geophysical Research*, 102(B9), 20199–20210. <https://doi.org/10.1029/97jb00957>
- Einsle, J. F., Eggeman, A. S., Martineau, B. H., Saghi, Z., Collins, S. M., Blukis, R., et al. (2018). Nanomagnetic properties of the meteorite cloudy zone. *Proceedings of the National Academy of Sciences of the United States of America*, 115(49), E11436–E11445. <https://doi.org/10.1073/pnas.1809378115>
- El Goresy, A., Zinner, E., Pellas, P., & Caillet, C. (2005). A menagerie of graphite morphologies in the Acapulco meteorite with diverse carbon and nitrogen isotopic signatures: Implications for the evolution history of acapulcoite meteorites. *Geochimica et Cosmochimica Acta*, 69(18), 4535–4556. <https://doi.org/10.1016/j.gca.2005.03.051>
- Fu, R. R., Lima, E. A., Volk, M. W. R., & Trubko, R. (2020). High-sensitivity moment magnetometry with the quantum diamond microscope. *Geochemistry, Geophysics, Geosystems*, 21(8), e2020GC009147. <https://doi.org/10.1029/2020gc009147>
- Fu, R. R., Weiss, B. P., Lima, E. A., Harrison, R. J., Bai, X.-N., Desch, S. J., et al. (2014). Solar nebula magnetic fields recorded in the Semarkona meteorite. *Science*, 346(6213), 1089–1092. <https://doi.org/10.1126/science.1258022>
- Garrick-Bethell, I., & Weiss, B. P. (2010). Kamacite blocking temperatures and applications to lunar magnetism. *Earth and Planetary Science Letters*, 294(1), 1–7. <https://doi.org/10.1016/j.epsl.2010.02.013>
- Garrick-Bethell, I., Weiss, B. P., Shuster, D. L., & Buz, J. (2009). Early lunar magnetism. *Science*, 323(5912), 356–359. <https://doi.org/10.1126/science.1166804>
- Gattacceca, J., Boustie, M., Hood, L., Cuq-Lelandais, J. P., Fuller, M., Bezaeva, N. S., et al. (2010). Can the lunar crust be magnetized by shock: Experimental groundtruth. *Earth and Planetary Science Letters*, 299(1–2), 42–53. <https://doi.org/10.1016/j.epsl.2010.08.011>
- Gattacceca, J., & Rochette, P. (2004). Toward a robust normalized magnetic paleointensity method applied to meteorites. *Earth and Planetary Science Letters*, 227(3–4), 377–393. <https://doi.org/10.1016/j.epsl.2004.09.013>
- Gattacceca, J., Suavet, C., Rochette, P., Weiss, B. P., Winkhofer, M., Uehara, M., & Friedrich, J. M. (2014). Metal phases in ordinary chondrites: Magnetic hysteresis properties and implications for thermal history. *Meteoritics & Planetary Sciences*, 49(4), 652–676. <https://doi.org/10.1111/maps.12268>
- Glenn, D. R., Fu, R. R., Kehayias, P., Sage, D. L., Lima, E. A., Weiss, B. P., & Walsworth, R. L. (2017). Micrometer-scale magnetic imaging of geological samples using a quantum diamond microscope. *Geochemistry, Geophysics, Geosystems*, 18(8), 3254–3267. <https://doi.org/10.1002/2017gc006946>
- Golabek, G. J., Bourdon, B., & Gerya, T. V. (2014). Numerical models of the thermomechanical evolution of planetesimals: Application to the acapulcoite-lodranite parent body. *Meteoritics & Planetary Sciences*, 49(6), 1083–1099. <https://doi.org/10.1111/maps.12302>
- Goldstein, J. I., & Michael, J. R. (2006). The formation of plessite in meteoritic metal. *Meteoritics & Planetary Sciences*, 41(4), 553–570. <https://doi.org/10.1111/j.1945-5100.2006.tb00482.x>
- Göpel, C., & Manhès, G. (2010). The thermal history of the Acapulco meteorite and its parent body deduced from U/Pb systematics in mineral separates and bulk rock fragments. *Comptes Rendus Geoscience*, 342(1), 53–59. <https://doi.org/10.1016/j.crte.2009.10.013>

- Greenwood, R. C., Burbine, T. H., Miller, M. F., & Franchi, I. A. (2017). Melting and differentiation of early-formed asteroids: The perspective from high precision oxygen isotope studies. *Geochemistry*, 77(1), 1–43. <https://doi.org/10.1016/j.chemer.2016.09.005>
- Greenwood, R. C., Franchi, I. A., Gibson, J. M., & Benedix, G. K. (2012). Oxygen isotope variation in primitive achondrites: The influence of primordial, asteroidal and terrestrial processes. *Geochimica et Cosmochimica Acta*, 94, 146–163. <https://doi.org/10.1016/j.gca.2012.06.025>
- Harrison, R. J., & Feinberg, J. M. (2008). FORCinel: An improved algorithm for calculating first-order reversal curve distributions using locally weighted regression smoothing. *Geochemistry, Geophysics, Geosystems*, 9(5). <https://doi.org/10.1029/2008gc001987>
- Keil, K., & McCoy, T. J. (2018). Acapulcoite-lodranite meteorites: Ultramafic asteroidal partial melt residues. *Geochemistry*, 78(2), 153–203. <https://doi.org/10.1016/j.chemer.2017.04.004>
- Khokhlov, A., & Hulot, G. (2015). Principal component analysis of palaeomagnetic directions: Converting a maximum angular deviation (MAD) into an α_{95} angle. *Geophysical Journal International*, 204(1), 274–291. <https://doi.org/10.1093/gji/ggv451>
- Kirschvink, J. L. (1980). The least-squares line and plane and the analysis of palaeomagnetic data. *Geophysical Journal International*, 62(3), 699–718. <https://doi.org/10.1111/j.1365-246x.1980.tb02601.x>
- Lappe, S. L. L., Church, N. S., Kasama, T., da Silva Fanta, A. B., Bromiley, G., Dunin-Borkowski, R. E., et al. (2011). Mineral magnetism of dusty olivine: A credible recorder of pre-accretionary remanence. *Geochemistry, Geophysics, Geosystems*, 12(12), Q12Z35. <https://doi.org/10.1029/2011gc003811>
- Lappe, S. L. L., Feinberg, J. M., Muxworthy, A. R., & Harrison, R. J. (2013). Comparison and calibration of nonheating paleointensity methods: A case study using dusty olivine. *Geochemistry, Geophysics, Geosystems*, 14(7), 2143–2158. <https://doi.org/10.1002/ggge.20141>
- Lima, E. A., & Weiss, B. P. (2016). Ultra-high sensitivity moment magnetometry of geological samples using magnetic microscopy. *Geochemistry, Geophysics, Geosystems*, 17(9), 3754–3774. <https://doi.org/10.1002/2016gc006487>
- Lucas, M. P., Dygert, N., Ren, J., Hesse, M. A., Miller, N. R., & McSweeney, H. Y. (2022). Thermochemical evolution of the acapulcoite-lodranite parent body: Evidence for fragmentation-disrupted partial differentiation. *Meteoritics & Planetary Sciences*, 57(12), 2248–2275. <https://doi.org/10.1111/maps.13930>
- Mansbach, E. N., Shah, J., Williams, W., Maurel, C., Bryson, J. F. J., & Weiss, B. P. (2022). Size ranges of magnetic domain states in tetraenaite. *Geochemistry, Geophysics, Geosystems*, 23(11). <https://doi.org/10.1029/2022gc010631>
- Mansbach, E. N., Weiss, B. P., Schnepf, N. R., Lima, E. A., Borlina, C. S., Chatterjee, N., et al. (2023). Magnetism of the acapulco primitive achondrite and implications for the evolution of partially differentiated bodies. *Magnetics Information Consortium (MagIC)*. <https://doi.org/10.7288/V4/MAGIC/19872>
- Maurel, C., Bryson, J. F. J., Lyons, R. J., Ball, M. R., Chopdekar, R. V., Scholl, A., et al. (2020). Meteorite evidence for partial differentiation and protracted accretion of planetesimals. *Science Advances*, 6(30), eaba1303. <https://doi.org/10.1126/sciadv.aba1303>
- Maurel, C., Bryson, J. F. J., Shah, J., Chopdekar, R. V., T. Elkins-Tanton, L., A. Raymond, C., & Weiss, B. P. (2021). A long-lived planetesimal dynamo powered by core crystallization. *Geophysical Research Letters*, 48(6), e2020GL091917. <https://doi.org/10.1029/2020gl091917>
- Maurel, C., Weiss, B. P., & Bryson, J. F. J. (2019). Meteorite cloudy zone formation as a quantitative indicator of paleomagnetic field intensities and cooling rates on planetesimals. *Earth and Planetary Science Letters*, 513, 166–175. <https://doi.org/10.1016/j.epsl.2019.02.027>
- McClelland, E. (1996). Theory of CRM acquired by grain growth, and its implications for TRM discrimination and paleointensity determination in igneous rocks. *Geophysical Journal International*, 126(1), 271–280. <https://doi.org/10.1111/j.1365-246x.1996.tb05285.x>
- McCoy, T. J., Keil, K., Clayton, R. N., Mayeda, T. K., Bogard, D. D., Garrison, D. H., et al. (1996). A petrologic, chemical, and isotopic study of monometallic and comparison with other acapulcoites: Evidence for formation by incipient partial melting. *Geochimica et Cosmochimica Acta*, 60(14), 2681–2708. [https://doi.org/10.1016/0016-7037\(96\)00109-3](https://doi.org/10.1016/0016-7037(96)00109-3)
- McCoy, T. J., Keil, K., Muenow, D. W., & Wilson, L. (1997). Partial melting and melt migration in the acapulcoite-lodranite parent body. *Geochimica et Cosmochimica Acta*, 61(3), 639–650. [https://doi.org/10.1016/s0016-7037\(96\)00365-1](https://doi.org/10.1016/s0016-7037(96)00365-1)
- Muxworthy, A. R., & Roberts, A. P. (2007). First-order reversal curve (FORC) diagrams. In D. Gubbins & E. Herrero-Bervera (Eds.), *Encyclopedia of geomagnetism and paleomagnetism* (pp. 266–272). Springer Netherlands.
- Neumann, W., Henke, S., Breuer, D., Gail, H., Schwarz, W. H., Tieloff, M., et al. (2018). Modeling the evolution of the parent body of acapulcoites and lodranites: A case study for partially differentiated asteroids. *Icarus*, 311, 146–169. <https://doi.org/10.1016/j.icarus.2018.03.024>
- Nichols, C. I. O., Bryson, J. F. J., Blukis, R., Herrero-Albillos, J., Kronast, F., Rüffer, R., et al. (2020). Variations in the magnetic properties of meteoritic cloudy zone. *Geochemistry, Geophysics, Geosystems*, 21(2), e2019GC008798. <https://doi.org/10.1029/2019gc008798>
- Nichols, C. I. O., Krakow, R., Herrero-Albillos, J., Kronast, F., Northwood-Smith, G., & Harrison, R. J. (2018). Microstructural and paleomagnetic insight into the cooling history of the IAB parent body. *Geochimica et Cosmochimica Acta*, 229, 1–19. <https://doi.org/10.1016/j.gca.2018.03.009>
- Ohtani, E., Sakurabayashi, T., & Kurosawa, K. (2022). Experimental simulations of shock textures in bcc iron: Implications for iron meteorites. *Progress in Earth and Planetary Science*, 9(1), 24. <https://doi.org/10.1186/s40645-022-00482-7>
- Palme, H., Schultz, L., Spettel, B., Weber, H. W., Wänke, H., Michel-Levy, M. C., & Lorin, J. C. (1981). The Acapulco meteorite: Chemistry, mineralogy and irradiation effects. *Geochimica et Cosmochimica Acta*, 45(5), 727–752. [https://doi.org/10.1016/0016-7037\(81\)90045-4](https://doi.org/10.1016/0016-7037(81)90045-4)
- Renne, P. R. (2000). $^{40}\text{Ar}/^{39}\text{Ar}$ age of plagioclase from Acapulco meteorite and the problem of systematic errors in cosmochronology. *Earth and Planetary Science Letters*, 175(1–2), 13–26. [https://doi.org/10.1016/s0012-821x\(99\)00287-3](https://doi.org/10.1016/s0012-821x(99)00287-3)
- Rochette, P., Gattacceca, J., Bourot-Denise, M., Consolmagno, G., Folco, L., Kohout, T., et al. (2009). Magnetic classification of stony meteorites: 3. Achondrites. *Meteoritics & Planetary Sciences*, 44(3), 405–427. <https://doi.org/10.1111/j.1945-5100.2009.tb00741.x>
- Shah, J., Williams, W., Almeida, T. P., Nagy, L., Muxworthy, A. R., Kovács, A., et al. (2018). The oldest magnetic record in our solar system identified using nanometric imaging and numerical modeling. *Nature Communications*, 9(1), 1173. <https://doi.org/10.1038/s41467-018-03613-1>
- Stephenson, A. (1993). Three-axis static alternating field demagnetization of rocks and the identification of natural remanent magnetization, gyroremanent magnetization, and anisotropy. *Journal of Geophysical Research*, 98(B1), 373–381. <https://doi.org/10.1029/92jb01849>
- Suavet, C., Weiss, B. P., & Grove, T. L. (2014). Controlled-atmosphere thermal demagnetization and paleointensity analyses of extraterrestrial rocks. *Geochemistry, Geophysics, Geosystems*, 15(7), 2733–2743. <https://doi.org/10.1002/2013gc005215>
- Swartzendruber, L. J., Itkin, V. P., & Alcock, C. B. (1991). The Fe-Ni (iron-nickel) system. *Journal of Phase Equilibria*, 12(3), 288–312. <https://doi.org/10.1007/bf02649918>
- Tauxe, L. (2010). *Essentials of paleomagnetism*. University of California Press.
- Tauxe, L., & Staudigel, H. (2004). Strength of the geomagnetic field in the Cretaceous normal superchron: New data from submarine basaltic glass of the Troodos ophiolite. *Geochemistry, Geophysics, Geosystems*, 5(2), Q02H06. <https://doi.org/10.1029/2003gc000635>
- Tikoo, S. M., Weiss, B. P., Buz, J., Lima, E. A., Shea, E. K., Melo, G., & Grove, T. L. (2012). Magnetic fidelity of lunar samples and implications for an ancient core dynamo. *Earth and Planetary Science Letters*, 337–338, 93–103. <https://doi.org/10.1016/j.epsl.2012.05.024>

- Touboul, M., Kleine, T., Bourdon, B., Van Orman, J. A., Maden, C., & Zipfel, J. (2009). Hf–W thermochronometry: II. Accretion and thermal history of the acapulcoite–lodranite parent body. *Earth and Planetary Science Letters*, 284(1–2), 168–178. <https://doi.org/10.1016/j.epsl.2009.04.022>
- Uehara, M., Gattacceca, J., Rochette, P., Demory, F., & Valenzuela, E. M. (2012). Magnetic study of meteorites recovered in the atacama desert (Chile): Implications for meteorite paleomagnetism and the stability of hot desert surfaces. *Physics of the Earth and Planetary Interiors*, 200–201, 113–123. <https://doi.org/10.1016/j.pepi.2012.04.007>
- Vervelidou, F., Weiss, B. P., & Lacroix, F. (2023). Hand magnets and the destruction of ancient meteorite magnetism. *Journal of Geophysical Research: Planets*, 128(4), e2022JE007464. <https://doi.org/10.1029/2022je007464>
- Wang, H., Wang, J., Chen-Wiegart, Y. C., & Kent, D. V. (2015). Quantified abundance of magnetofossils at the Paleocene-Eocene boundary from synchrotron-based transmission X-ray microscopy. *Proceedings of the National Academy of Sciences of the United States of America*, 112(41), 12598–12603. <https://doi.org/10.1073/pnas.1517475112>
- Wang, H., Weiss, B. P., Bai, X. N., Downey, B. G., Wang, J., Wang, J., et al. (2017). Lifetime of the solar nebula constrained by meteorite paleomagnetism. *Science*, 355(6325), 623–627. <https://doi.org/10.1126/science.aaf5043>
- Weisberg, M. W., McCoy, T. J., & Krot, A. N. (2006). Systematics and evaluation of meteorite classification. In *Meteorites and the early solar system II*.
- Weiss, B. P., Berdahl, J. S., Elkins-Tanton, L., Stanley, S., Lima, E. A., & Carporzen, L. (2008). Magnetism on the angrite parent body and the early differentiation of planetesimals. *Science*, 322(5902), 713–716. <https://doi.org/10.1126/science.1162459>
- Weiss, B. P., & Elkins-Tanton, L. T. (2013). Differentiated planetesimals and the parent bodies of chondrites. *Annual Review of Earth and Planetary Sciences*, 41(1), 529–560. <https://doi.org/10.1146/annurev-earth-040610-133520>
- Weiss, B. P., Gattacceca, J., Stanley, S., Rochette, P., & Christensen, U. R. (2010). Paleomagnetic records of meteorites and early planetesimal differentiation. *Space Science Reviews*, 152(1–4), 341–390. <https://doi.org/10.1007/s11214-009-9580-z>
- Weiss, B. P., Lima, E. A., Fong, L. E., & Baudenbacher, F. J. (2007). Paleomagnetic analysis using SQUID microscopy. *Journal of Geophysical Research*, 112(B9). <https://doi.org/10.1029/2007jb004940>
- Yang, J., & Goldstein, J. I. (2004). Magnetic contribution to the interdiffusion coefficients in bcc (α) and fcc (γ) Fe–Ni alloys. *Metallurgical and Materials Transactions A*, 35(6), 1681–1690. <https://doi.org/10.1007/s11661-004-0077-9>
- Yang, J., & Goldstein, J. I. (2005). The formation of the Widmanstätten structure in meteorites. *Meteoritics & Planetary Sciences*, 40(2), 239–253. <https://doi.org/10.1111/j.1945-5100.2005.tb00378.x>
- Yang, J., Goldstein, J. I., & Scott, E. R. D. (2007). Iron meteorite evidence for early formation and catastrophic disruption of protoplanets. *Nature*, 446(7138), 888–891. <https://doi.org/10.1038/nature05735>
- Yu, Y., Tauxe, L., & Gee, J. S. (2007). A linear field dependence of thermoremanence in low magnetic fields. *Physics of the Earth and Planetary Interiors*, 162(3), 244–248. <https://doi.org/10.1016/j.pepi.2007.04.008>
- Zipfel, J., Palme, H., Kennedy, A. K., & Hutcheon, I. D. (1995). Chemical composition and origin of the Acapulco meteorite. *Geochimica et Cosmochimica Acta*, 59(17), 3607–3627. [https://doi.org/10.1016/0016-7037\(95\)00226-p](https://doi.org/10.1016/0016-7037(95)00226-p)

References From the Supporting Information

- Bland, P., Zolensky, M., Benedix, G., & Sephton, M. (2006). Weathering of chondritic meteorites. *Meteorites and the Early Solar System II*, 1, 853–867.
- Boland, J. N., & Duba, A. (1981). Solid-state reduction of iron in olivine–planetary and meteoritic evolution. *Nature*, 294(5837), 142–144. <https://doi.org/10.1038/294142a0>
- Dunlop, D., & Özdemir, Ö. (1997). *Rock magnetism: Fundamentals and Frontiers* (1 ed.). Cambridge University Press.
- Leroux, H., Libourel, G., Lemelle, L., & Guyot, F. (2003). Experimental study and REM characterization of dusty olivines in chondrites: Evidence for formation by in situ reduction. *Meteoritics & Planetary Sciences*, 38(1), 81–94. <https://doi.org/10.1111/j.1945-5100.2003.tb01047.x>
- Uehara, M., Beek, C. J., Gattacceca, J., Skidanov, V. A., & Quesnel, Y. (2010). Advances in magneto-optical imaging applied to rock magnetism and paleomagnetism. *Geochemistry, Geophysics, Geosystems*, 11(5). <https://doi.org/10.1029/2009gc002653>
- Williams, G. M., & Pavlovic, A. S. (1968). The magnetostriction behavior of iron single crystals. *Journal of Applied Physics*, 39(2), 571–572. <https://doi.org/10.1063/1.2163525>
- Werwiński, M., & Marciniak, W. (2017). Ab initio study of magnetocrystalline anisotropy, magnetostriction, and fermi surface of Li_0FeNi (tetra-tenite). *Journal of Physics D: Applied Physics*, 50(49), 495008. <https://doi.org/10.1088/1361-6463/aa958a>

Journal of Geophysical Research: Planets

Supporting Information for

Magnetism of the Acapulco Primitive Achondrite and Implications for the Evolution of Partially Differentiated Bodies

Elias N. Mansbach¹, Benjamin P. Weiss¹, Neesha R. Schnepf², Eduardo A. Lima¹, Cauê S. Borlina^{1,3}, Nilanjan Chatterjee¹, Jérôme Gattacceca⁴, Minoru Uehara⁴, Huapei Wang⁵

¹*Department of Earth, Atmosphere, and Planetary Sciences, Massachusetts Institute of Technology, Cambridge, MA, USA*

²*Laboratory for Atmospheric and Space Physics, University of Colorado, Boulder, CO, USA*

³*Department of Earth and Planetary Science, Johns Hopkins University, Baltimore, MD, USA*

⁴*CNRS, Aix Marseille Université, IRD, INRAE, CEREGE, Aix-en-Provence, France*

⁵*School of Geophysics and Geomatics, China University of Geosciences, Wuhan, China*

Contents of this file

*Text S1 to S5
Figures S1 to S12
Tables S1 to S3
Data Sets S1 to S2
References*

Introduction

This supplement provides data associated with sample preparation, metal bearing silicate (MBS) inclusion grain morphologies, and additional rock magnetism measurements not shown in the main text. In particular, following an explanation of how samples were cut, extracted, and prepared for measurement, we show high-resolution transmission X-ray microscope images of MBS inclusions. We then provide further evidence for tetrataenite in Acapulco via magneto-optical imaging (MOI) data. We also present quantum diamond microscope (QDM) images of the interstitial metal grains in bulk samples and metal inclusions in MBSs. Lastly, we provide orthographic projections of the alternating field (AF) demagnetization of natural remanent magnetization (NRM) for all bulk samples and MBSs not shown in the main text.

S1 Sample Preparation.

We cut bulk samples off the main mass provided by the Smithsonian (USNM 5967) in the MIT magnetically shielded room using a diamond wire saw lubricated with ethanol to minimize oxidation. Three transects were made perpendicular to the fusion crust to sample both the fusion crust and the interior (Fig. S1). Two of the transects were further cut into four subsamples each (NMMAC1, 2, 3, and 4 from the first transect and NMMAC5, 6, 7, 8 from the second). The fusion-crust exterior of the third transect was isolated and cut to create an additional fusion-crust sample (NMMAC12). After cutting, each subsample was glued onto a HCl-acid cleaned and demagnetized Ge 124 quartz disk (moment $<1 \times 10^{-11} \text{ Am}^2$) with nonmagnetic cyanoacrylate for measurement.

We extracted individual MBSs for paleomagnetic study following the experimental methods in Borlina et al. (2021). A $\sim 300 \mu\text{m}$ thick section, called NMMAC11 (Fig. S2), was cut using a diamond wire saw and embedded in epoxy. We then polished the section down to a thickness of $200 \mu\text{m}$, which is approximately equal to the diameter of an average-sized silicate grain in Acapulco. We then identified MBSs using reflected light microscopy (Fig. S3). We isolated MBSs from the surrounding matrix using a demagnetized drill bit and extracted them by gluing an acid-washed quartz glass holder to the top of the grain using cyanoacrylate cement. The MBSs were then extracted and glued using cyanoacrylate cement to a HCl-acid quartz disk for magnetic measurements. We recorded the orientations of the MBSs prior to and after extraction to maintain mutually oriented samples through the experiment to an uncertainty of $<5^\circ$.

S2 Morphology and Inclusions in MBSs

We used transmission X-ray microscope (TXM) images of an MBS to study the morphologies and sizes of the metal inclusions at the National Synchrotron Light Source II (Beamline X8C) at Brookhaven National Laboratory (beam energy 7.2 keV) (Wang et al., 2015). The MBS, which had a piece of metal attached to it ($\sim 0.5 \text{ mm}$ total width), was mounted on a tungsten carbide pin for imaging from the front and side separately. The energy was chosen to be just higher than the iron absorption K-edge of 7.112 keV to maximize X-ray absorption (Wang et al., 2015). Analysis of grain morphology from TXM images was done using ImageJ.

TXM images (Fig. S4a) of the metal inclusions in an MBS show two distinct clusters of grains, labeled Cluster 1 and Cluster 2. Both clusters have a range of morphologies from nearly equant grains to needle-like, elongated grains. The average elongated axis directions of Cluster 1 and Cluster 2 are $37.0^\circ \pm 28.8^\circ (1\sigma)$ and $64.9^\circ \pm 26.6^\circ (1\sigma)$, respectively (Fig. S4b). This is consistent with previous reports that the metal grains in MBSs seem to have a preferred orientation, potentially aligned with the silicate crystal axes, which in turn may have been inherited from precursor silicate grains (McCoy

et al., 2019). The metal inclusions vary in diameter from 0.4 to <13 μm , with just over half of the grains falling below 2 μm (Fig. S4c). No difference in grain size distribution is observed between the two clusters. The same is true for the inclusion aspect ratios, defined as the grain width divided by the length, of the two clusters, with each having a mean ratio of 0.65 ± 0.21 (1σ) (Fig. S4d). The most elongated grain amongst the two clusters has an aspect ratio of 0.17.

Dispersed μm -sized metal inclusions in MBSs (main text Fig. 1 insert) are reminiscent of metal grains in dusty olivine chondrules [DOCs, see Fu et al. (2014) or Borlina et al. (2021)]. However, the texture and compositions of the inclusions in Acapulco differ (McCoy et al., 2019). DOCs, which formed from the subsolidus reduction of fayalitic olivine (Boland & Duba, 1981), have inclusions scattered throughout the chondrule and tend to be nearly pure iron (Fu et al., 2014; Leroux et al., 2003). MBSs in ALs have metal inclusions typically localized in the centers of the silicate grains (< ~66% of grain radius, but perhaps not extending to grain center) and have Ni abundances from 4.5 to 32.1 wt.% (McCoy et al., 2019). Sulfides are also found in MBSs, but not in DOCs. While it has been proposed that MBSs in ALs formed via olivine reduction while the chondrules were in the nebula (Zipfel et al., 1995), another hypothesis is that they formed via the trapping of Fe-Ni-S melts during silicate grain growth during metamorphism (El Goresy et al., 2005). However, the presence of metal inclusions in relict chondrules in the Grove Mountains 020043 acapulcoite, which experienced minimal to no partial melting, suggests that the metal grains were trapped during chondrule crystallization and therefore inherited from the parent chondrite (McCoy et al., 2019).

S3 Magnetic Measurements

S3.1 MOI

We used MOI imaging to assess whether and where cloudy zone microstructures and tetrataenite are present in Acapulco interstitial metal. MOI images the out-of-the-plane magnetic field of a planar sample via its Faraday effect on linearly polarized lights threading a thin garnet film on top of the sample (Uehara et al., 2010). The brightest regions in MOI images of metal-bearing meteorites are typically associated with cloudy zone tetrataenite and less bright areas are associated with plessite, while weak or no brightness is typically associated with kamacite and martensite (Uehara et al., 2011). Given that all of these minerals have saturation isothermal remanent magnetizations (IRM) that are within a factor of 3 of each other, these variations in MOI intensity have been attributed to be mainly a reflection of the mean magnetization over ~10 μm and therefore the domain state of the grains, with single domain (SD) grains having the strongest signal, pseudo single domain (PSD) grains having weaker signal, and multidomain grains having no detectable signal. MOI images can also be used to assess coercivity through the application of backfield IRMs and looking for the remaining signal. Cloudy zone tetrataenite retains a signal after back field IRM applications to ~1 T after an initial 3 T application (Uehara et al., 2011). Comparatively, grains with coercivities 250 – 400 mT are consistent with the presence of μm -sized tetrataenite in plessite (Uehara et al., 2011).

MOI of Acapulco thin section USNM 5967-1 was performed at CEREGE following the methodology of Uehara et al. (2010). A 1 T out-of-the-plane (z) IRM was applied to the thin section and analyzed with MOI followed by a back field IRM applications of 300 mT. After the 1 T IRM application, we observed signals on the rims on interstitial metals grains (Fig. S5b) indicative of strongly magnetic ferromagnetic phases (e.g., fine-grained tetrataenite). However, after a backfield IRM application of 300 mT (Fig. S5c), the signals mostly disappeared except for some originating from segments of the rim. Due to the low coercivity of the rims, we interpret them to not be consistent with cloudy zone tetrataenite. Further BSE and SE imaging of the grains indicates the presence of a high-Ni rim, about 200 nm in width collocated with the MOI signal (Fig. S6). The composition of the rim alone cannot be determined due to its small width. However, EDS spot measurements of area just interior to the rim provided a composition of 42 wt.% Ni, indicating that the rim itself, which

should be enriched in Ni compared to the interior, may be 50 wt.% Ni. We interpret these narrow rims to be tetrataenite on account of their composition and regions with coercivities greater than 300 mT.

While MBSs were not the target of the MOI images, there are multiple MBSs in the MOI view in Fig. S5. We note that one of the MBSs, which is outlined with the white box in Fig. S5A, showed a signal after the 1 T IRM application, albeit weaker than the rims discussed above. After the 300 mT backfield application, the signal disappeared, again indicating a lack of cloudy zone tetrataenite.

S3.2 Identification of Tetrataenite Through Sample Heating.

A powerful way to assess the presence of tetrataenite is to heat the sample to above the tetrataenite disordering temperature. Samples with tetrataenite that undergo thermally-induced disordering will exhibit large drops in coercivity. Although taenite orders to tetrataenite during slow cooling at 320°C, its disordering temperature as observed during the short (minutes to hours) timescales of laboratory heating is typically higher (in the range of 500-600°C) due to kinetic inhibition (Dos Santos et al., 2015). For example, the Gudder LL5 and Pê L6 ordinary chondrites display peaks in their coercivity spectra (derivative of magnetization with respect to applied IRM field, dM/dB) at ~700 mT [see Fig. 10 in Gattacceca et al. (2014)]. Heating of Pê to 450°C for 20 minutes produced little change in its magnetic properties, as expected due to the limited tetrataenite disordering, while heating to 600°C for 20 minutes resulted in a complete loss of the ~700 mT peak as the tetrataenite fully disordered (Gattacceca et al., 2014).

To search for tetrataenite in Acapulco, we conducted an analogous experiment on bulk interior Acapulco sample NMMAC7. Following Gattacceca et al. (2014), we performed IRM acquisition on the sample up to 2.7 T. We then heated the sample to 450°C and 600°C for 20 minutes each, performing IRM acquisition after each of these heating steps.

The IRM acquisition data on NMMAC7 prior to heating (Fig. S7a) show that the sample reached saturation remanent magnetization at ~940 mT. After heating to 450°C, the sample acquired IRM at a faster rate at fields below 800 mT but did not reach saturation until ~940 mT. After heating to 600°C, the sample reached saturation at ~570 mT. The large change in saturating IRM field from pre-heating and 450°C to 600°C is expected for tetrataenite that underwent progressive thermal disordering. It should be noted that there is no observed peak >100 mT in the coercivity dM/dB spectra (Fig. S7b) as seen in some ordinary chondrites (Gattacceca et al., 2014). This is likely because the bulk Acapulco sample magnetizations are dominated by the multidomain, interstitial metal grains as discussed in the main text.

S3.3 FORC Diagram Parameters

The corrections and smoothing parameters used to make the FORC diagrams via FORCinel (Harrison & Feinberg, 2008) in Fig. 8 in the main text are as follows:

- Drift Correct SF = 5
- Remove first/last point = true
- Slope correct and normalize (85%): true
- Subtract lower branch: 2
- Gridded: false
- VARIFORC smoothing: Sc0 = 4, Sc1 = 7, Sb0 = 4, Sb1 = 7, lambda = 0.2, output = 1.

The raw data for the two FORC diagrams can be found in Data Set S1 and S2.

S3.4 Quantum Diamond Microscope (QDM) Images.

The location and distribution of the magnetic remanence carriers in MBSs were determined using a QDM in the MIT Paleomagnetism Laboratory. The QDM maps the magnetic field with a ~5 µm spatial resolution at a distance of ~10 µm above the sample [moment sensitivity $1 \cdot 10^{-14} \text{ Am}^2$ (Fu

et al., 2020; Glenn et al., 2017)]. Combined with optical images acquired by the QDM, these maps enabled us to determine the location of the ferromagnetic carriers and to establish whether magnetization was carried in the interior of the MBSs and likely to be primary rather than from contamination on the edges of the grains or from any alteration products produced during terrestrial weathering. We additionally created QDM maps of the interstitial metal grains in thin section USNM 5967-1. However, to avoid saturation of the QDM, the maps had to be taken at a distance of 120 μm .

The QDM map of a 0.5 T IRM applied to Acapulco thin section USNM 5967-1 taken 120 μm above the sample shows that the strongest magnetic fields are located above the interstitial metal grains (Fig. S8a, b). As expected for nonferromagnetic minerals, the troilite (FeS) grains do not have a magnetic signal (Fig. S8c). A highlighted MBS grain adjacent to an interstitial metal grain outlined does show a magnetic field collocated above the metal inclusions (Fig. S8c). However, that field is ~ 7.5 times weaker than the field above the interstitial metal grain.

The QDM maps of a 1 T IRM applied to two MBSs shows that the magnetic fields produced by the samples are collocated with the metal inclusions (Fig. S8f, h), similar to what was found for the adjacent MBS in the thin section in Fig. S8A. No magnetic signature was found outside of the grains, indicating that the magnetizations of the MBSs are carried by the inclusions alone and not contamination from the any residual pieces of surrounding grains that may have adhered to the MBSs during extraction or from alteration rinds due to terrestrial weathering (Bland et al., 2006).

S3.5 AF Demagnetization of ARM.

AF demagnetization of an ARM (200 μT bias field, 260 mT AC field) applied to MBS5 is noisy similar to NRM demagnetization, though the ARM is quickly demagnetized at AF values < 80 mT compared to the NRM (Fig. S9). The AF demagnetization of ARM in MBS5 does not show a consistent loss in moment after 125 mT. Comparatively, the ARM AF demagnetizations of a synthetic DOC and LL DOC show smoother losses in moment as the samples are progressively demagnetized.

S3.6 ARM and IRM Acquisition.

To determine the fidelity of the samples to acquire a TRM in the presence of a background field and to identify any magnetic anisotropy, we calculated the angle between the ARM gained and the direction of the bias field, defined as

$$\Delta\theta_{\text{ARM}} = \cos^{-1} \left(\frac{(\mathbf{M}_{\text{ARM}} - \mathbf{M}_{\text{demagnetized}}) \cdot [\mathbf{0} \ 0 \ 1]}{\|\mathbf{M}_{\text{ARM}} - \mathbf{M}_{\text{demagnetized}}\|} \right),$$

where \mathbf{M}_{ARM} is the magnetization vector after ARM application and $\mathbf{M}_{\text{demag}}$ is the magnetization vector after the sample is fully demagnetized (i.e., to AF level of 130 mT). We use ARM as an analog for TCRM (D. J. Dunlop & Argyle, 1997). To diagnose magnetic anisotropy that could affect NRM demagnetizations and recording properties, we additionally measured the angle between the IRM gained by the bulk samples and MBSs relative to the magnetizing field direction, $\Delta\theta_{\text{IRM}}$. This angle is defined in the same way as $\Delta\theta_{\text{ARM}}$ above but with “ARM” replaced by “IRM”.

The angles between the bias field direction and the ARM ($\Delta\theta_{\text{ARM}}$) and IRM ($\Delta\theta_{\text{IRM}}$) gained by the bulk samples are essentially indistinguishable for fusion-crust and interior samples (Fig. S10a): for two fusion-crust samples, NMMAC5 and NMMAC12, $\Delta\theta_{\text{ARM}}$ is 15.2° and 21.7° respectively, while for the interior samples, $\Delta\theta_{\text{ARM}}$ ranges from 4.0° to 25.6°. The large difference in bias field direction and ARM gained suggests the presence of magnetic anisotropy, spurious remanence from the AC field, or that the metal inclusions in MBS and plessite have coercivities larger than the 145 mT AC field. Repeated ARM applications to NMMAC4 (Fig. S10c) produced scattered directions and magnitudes for the gained magnetization, indicating spurious remanence. IRM application results in $\Delta\theta_{\text{IRM}}$ values of 4.5° and 21.3° for the NMMAC1 and NMMAC12 fusion-crust samples,

respectively, and 10.3° and 5.2° for the NMMAC6 and NMMAC7 interior samples, respectively (Fig. S10b).

Application of a 200 μ T ARM to MBS2 and MBS5 (145 mT AC field) resulted in $\Delta\theta_{\text{ARM}}$ values of 78° and 42° respectively (Fig. S10d). The large angular deviations may be due to a large ARM anisotropy, spurious ARM from the AC field, or that the metal inclusions have larger coercivities than the 145 mT AC field. The last explanation is possibly consistent with the results of the IRM demagnetizations that suggested MBSs have grains with coercivities larger than 145 mT as 20-40% of the normalized IRMs were still present after 145 mT (main text Fig. 7A). The $\Delta\theta_{\text{IRM}}$ values were 17.2°, 3.4°, and 12.9° for MBS8, MBS4, and MBS5 respectively. The large angular deviations from the external field direction suggests the presence of a magnetic anisotropy in MBSs, which is also supported by the common elongation axis seen in TXM images (Fig. S4).

S4 Tables of Rock Magnetic Properties.

The rock magnetic properties and sample descriptions of the bulk samples and MBSs are shown in Table S1 and Table S2, respectively.

S5 Natural Remanent Magnetization

S5.1 Bulk Samples.

Orthographic projections of all AF demagnetizations for bulk sample NRM are shown in Fig. S11. Grey arrows represent low coercivity (LCi and LCf) components and peach-colored arrows represent medium coercivity (MCi and MCf) components. Note that two bulk samples, NMMAC2 and NMMAC7, have only an LCi component, and NMMAC8 had two MCi components. The demagnetization behavior at applied fields above the MCi/MCf component is labeled the high coercivity (HC) range. All component directions and maximum angular deviations were calculated using principal component analysis (PCA) (Kirschvink, 1980). See Table S3 for the inclination, declination, and maximum angular deviation for the LCi/LCf and MCi/MCf components. No components were anchored to the origin, and we assessed if a component could be considered origin-trending based on the DANG-MAD test discussed in the main text.

NMMAC1. Sample NMMAC1 is a fusion-crust sample with a mean distance of 1.36 mm into the interior. AF demagnetization of NRM identified an LCf and an MCf component. The LCf component unblocked between 0 and 4.5 mT and the MCf component unblocked between 5.5 and 29.0 mT. The HC range was defined to be all steps above the MCf component (30 to 85 mT).

NMMAC2. Sample NMMAC2 is an interior sample with a mean distance 3.83 mm from the fusion crust. AF demagnetization of NRM (Fig. S11a) identified an LCi component only. The LCi component unblocked between 0 and 5.5 mT. The HC range was defined to be all steps above the LCi component (6 to 85 mT).

NMMAC3. Sample NMMAC3 is an interior sample with a mean distance 5.89 mm from the fusion crust. AF demagnetization of NRM identified an LCi and an MCi component. The LCi component unblocked between 0 and 10 mT and the MCi component unblocked between 11 and 24.5 mT. The HC range was defined to be all steps above the MCi component (25 to 85 mT).

NMMAC4. Sample NMMAC4 is an interior sample with a mean distance 8.82 mm from the fusion crust. AF demagnetization of NRM (Fig. S11b) identified an LCi and an MCi component. The LCi component unblocked between 0 and 5 mT and the MCi component

unblocked between 5.5 and 10 mT. The HC range was defined to be all steps above the MCI component (11.5 to 85 mT).

NMMAC5. Sample NMMAC5 is a fusion-crust sample with a mean distance of 0.92 mm into the interior. AF demagnetization of NRM identified an LCf and an MCf component. The LCf component unblocked between 0 and 14 mT and the MCf component unblocked between 14.5 and 66 mT. The HC range was defined to be all steps above the MCf component (67 to 145 mT).

NMMAC6. Sample NMMAC6 is an interior sample with a mean distance 2.62 mm from the fusion crust. AF demagnetization of NRM (Fig. S11c) identified an LCI and an MCI component. The LCI component unblocked between 0 and 15 mT and the MCI component unblocked between 17.5 and 24.5 mT. The HC range was defined to be all steps above the MCI component (25 to 145 mT).

NMMAC7. Sample NMMAC7 is an interior sample with a mean distance 4.43 mm from the fusion crust. AF demagnetization of NRM identified an LCI component. The LCI component unblocked between 0 and 13 mT. The HC range was defined to be all steps above the LCI component (13.5 to 145 mT).

NMMAC8. Sample NMMAC8 is an interior sample with a mean distance 6.36 mm from the fusion crust. AF demagnetization of NRM (Fig. S11d) identified an LCI and two MC components. The LCI component unblocked between 0 and 12 mT and the MCI components unblocked between 12.5 and 17.5 mT and 18 and 28 mT. The HC range was defined to be all steps above the MCI components (29 to 85 mT).

NMMAC12. Sample NMMAC12 is a fusion crust sample with a mean distance of 1.0 mm into the interior. AF demagnetization of NRM (Fig. S11e) identified an LCf and an MCf component. The LCf component unblocked between 0 and 3 mT and the MCf component unblocked between 3.5 and 59 mT. The HC range was defined to be all steps above the Mf component (60 to 145 mT).

S5.2 MBSs

Orthographic projections of all AF demagnetizations for MBS NRMs are shown in Figure S12. No NRM components were observed in any of the demagnetizations with the exception of possible weak LC components in MBS3 and MBS9.

S6 Shock Remagnetization in Kamacite and Tetrataenite

In Section 2.1 in the main text, we note that since Acapulco did not experience a shock greater than 5 GPa (Palme et al., 1981), it is unlikely to have been remagnetized by shock or acquired a shock remanent magnetization. Here we show calculations that describe the necessary compressional pressures needed for shock anisotropy to overcome shape anisotropy and magnetocrystalline anisotropy for kamacite and tetrataenite respectively.

The magnetic energy density associated with stress follows (Tauxe, 2010):

$$\epsilon_{\sigma} = \frac{3}{2} \lambda \sigma [\sin \theta]^2$$

where λ is a stress constant, σ is the pressure, and θ is the angle between the applied stress and the crystallographic axis. The magnetic energy density for magnetocrystalline anisotropy follows (Tauxe, 2010):

$$\epsilon_M = K_1 [\sin \beta]^2$$

where K_1 is the magnetocrystalline energy constant and β is the angle relative to the easy axis. Lastly, the magnetic energy density for shape anisotropy follows (Tauxe, 2010):

$$\epsilon_S = \frac{1}{2} \mu_0 \Delta N M_s^2$$

where ΔN is the difference in demagnetization factors, which is a function of axial ratio, and M_s is the saturation magnetization.

For stress anisotropy to overcome magnetocrystalline and shape anisotropy, $\epsilon_\sigma > \epsilon_M, \epsilon_S$. Letting $\theta = \beta = 90^\circ$, we find that

$$\sigma > \frac{2K_1}{3\lambda}$$

and

$$\sigma > \frac{1}{3\lambda} \mu_0 \Delta N M_s^2$$

for magnetocrystalline and shape anisotropy respectively.

Tetrataenite is dominated by magnetocrystalline anisotropy and kamacite is dominated by shape anisotropy. Therefore, for magnetocrystalline anisotropy and tetrataenite [K_1 is $1.37 \times 10^6 \text{ J/m}^3$ (Einsle et al., 2018) and λ is 9.4×10^{-6} (Werwiński & Marciniak, 2017)], we find $\sigma > 97 \text{ GPa}$. For shape anisotropy and kamacite [λ is 2.5×10^{-5} (Williams & Pavlovic, 1968) and M_s is $1.715 \times 10^6 \text{ A/m}$ (D. Dunlop & Özdemir, 1997)], we find $\sigma > 49\Delta N \text{ GPa}$. For an axial ratio of 0.9 (nearly equant), at which point shape anisotropy is relevant for kamacite, ΔN is ~ 0.05 , and therefore $\sigma > 2.5 \text{ GPa}$. However, the average elongations of the grains observed in MBSs have an axial ratio of 0.65, which corresponds to $\sigma > 6.4 \text{ GPa}$. This is above the 5 GPa upper limit for Acapulco.

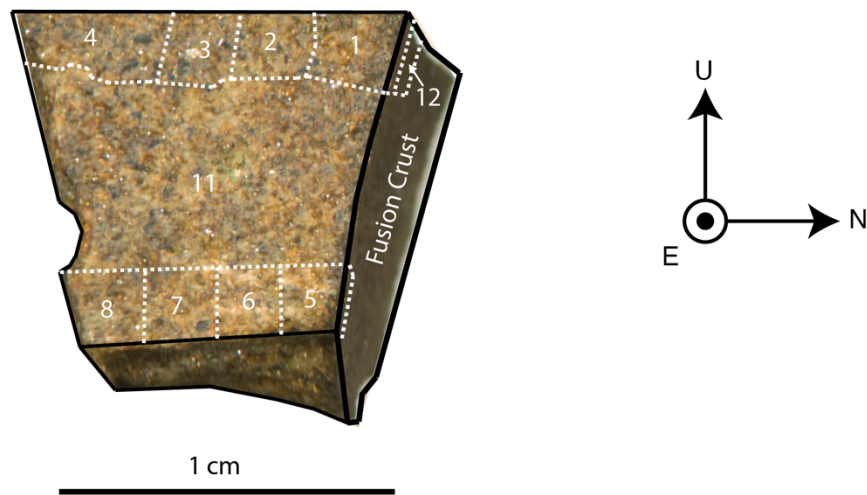


Figure S1. Locations of our subsamples in Acapulco sample USNM 5967 and orientation cube. Note that only the top surface shown in the drawing (east face) is to scale. The fusion crust is on the north face. The locations of the bulk samples cut from this main mass are indicated on the drawing, with NMMAC subsample numbers noted. Bulk sample NMMAC12 is located immediately under NMMAC1. NMMAC11 was polished down to a thickness of $\sim 200\ \mu\text{m}$ to create a thick section for MBS extraction.

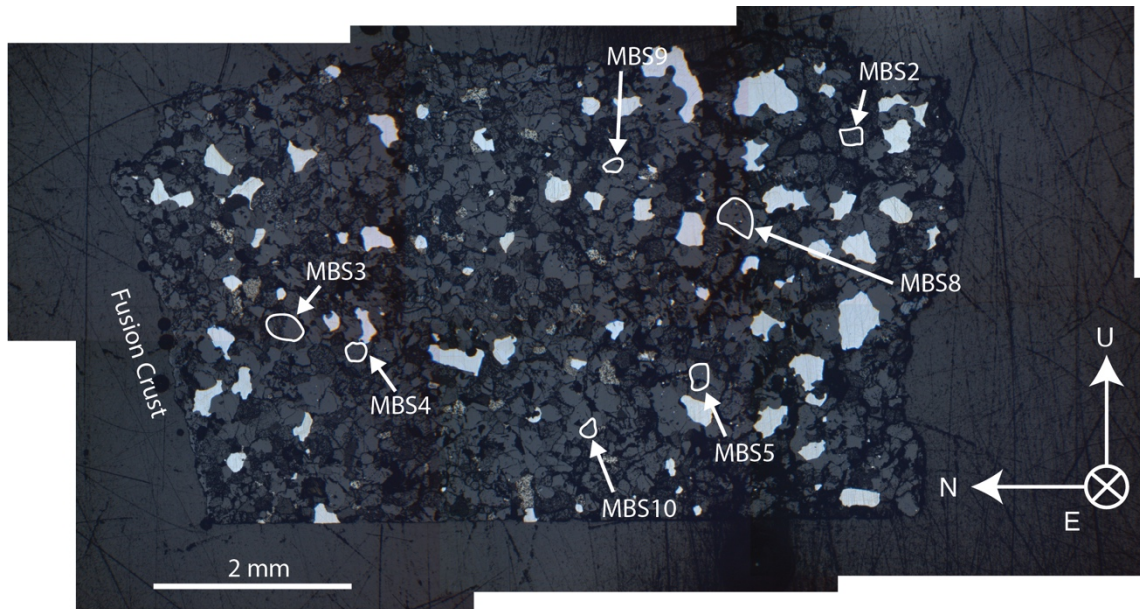


Figure S2. Composite reflected light microscope image of the thick section NMMAC11. The west face of NMMAC 11 is shown. The fusion crust is on the left side of the thick section. The locations of MBSs extracted for this study are labeled with arrows. The thick section was embedded in epoxy prior to MBS extraction.

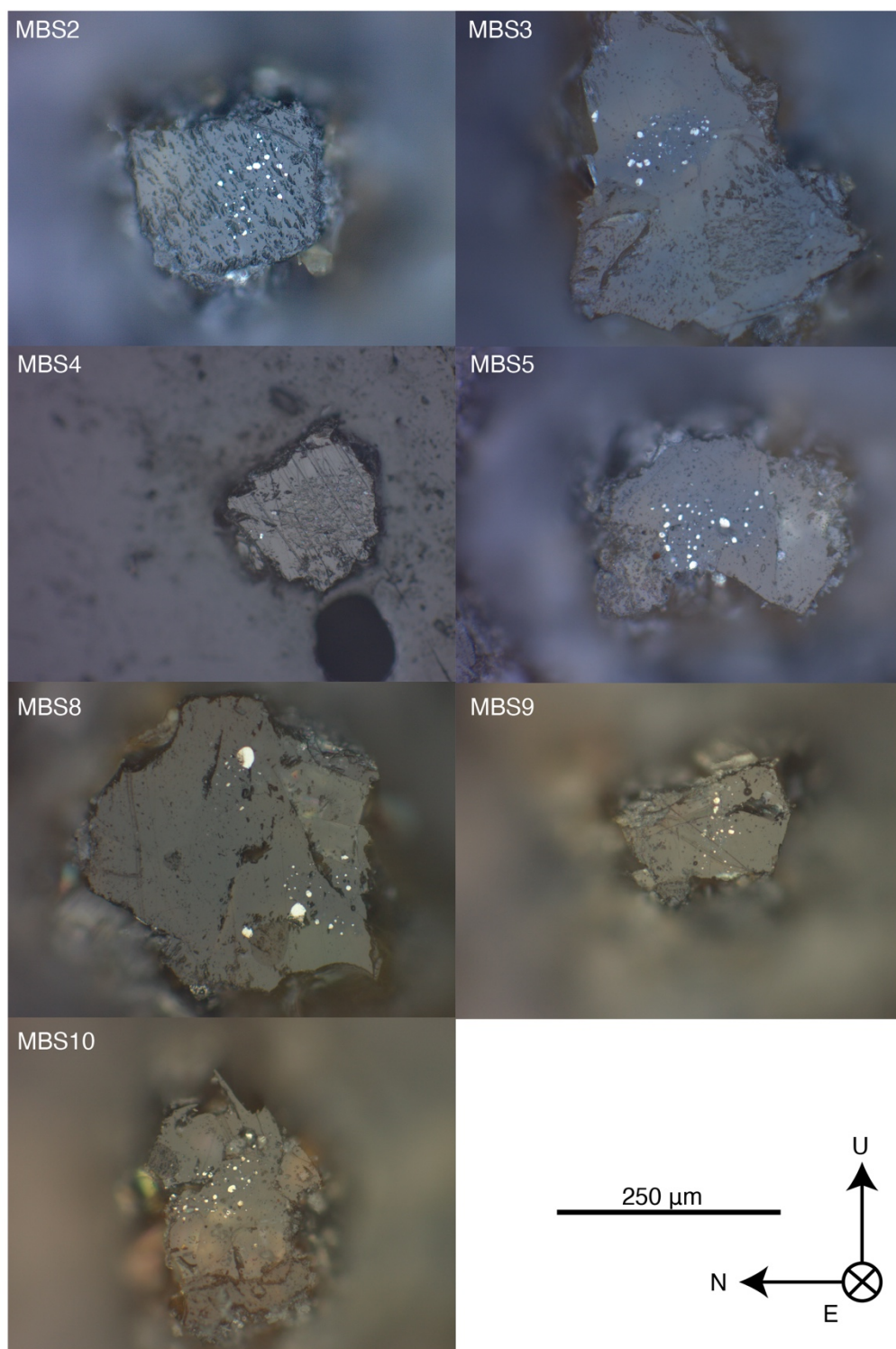


Figure S3. Reflected light images of MBSs. Each panel shows a reflected light image taken at 20× magnification of an MBS used in this study prior to extraction and after the surrounding grains were removed following the procedure in the supplement. The only

exception is MBS4, which was photographed after being embedded in epoxy. The metal inclusions are visible in the MBSs and tend to cluster in the core of the silicate.

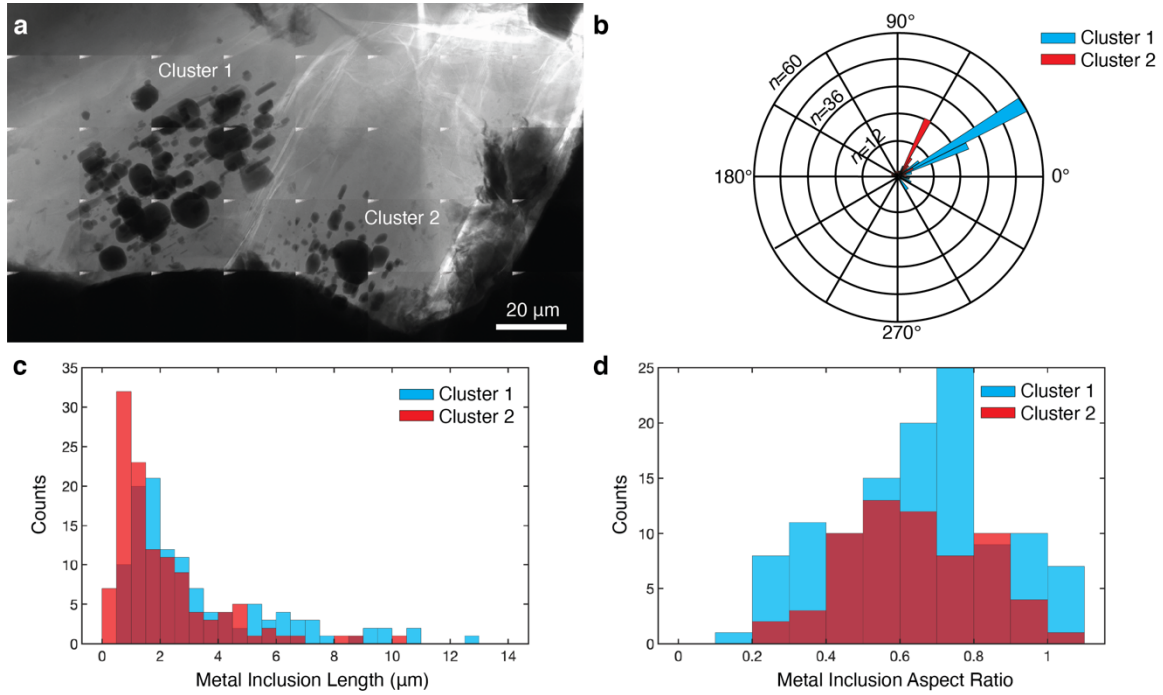


Figure S4. Analysis of MBS metal morphologies and sizes. **a)** Stitched TXM images of an MBS. There are two distinct clusters of metal inclusions, labeled Cluster 1 and Cluster 2. **b)** Rose diagram of the directions of the elongated axes in Clusters 1 and 2. Both clusters show little variability in their elongation direction. **c)** Histogram of the metal inclusion lengths for Clusters 1 and 2. Both clusters show a similar distribution of grain sizes. **d)** Histogram of the axial ratio (grain width to length) of the metal inclusions. An axial ratio of 1 corresponds to a sphere while an axial ratio of 0 corresponds to a plane.

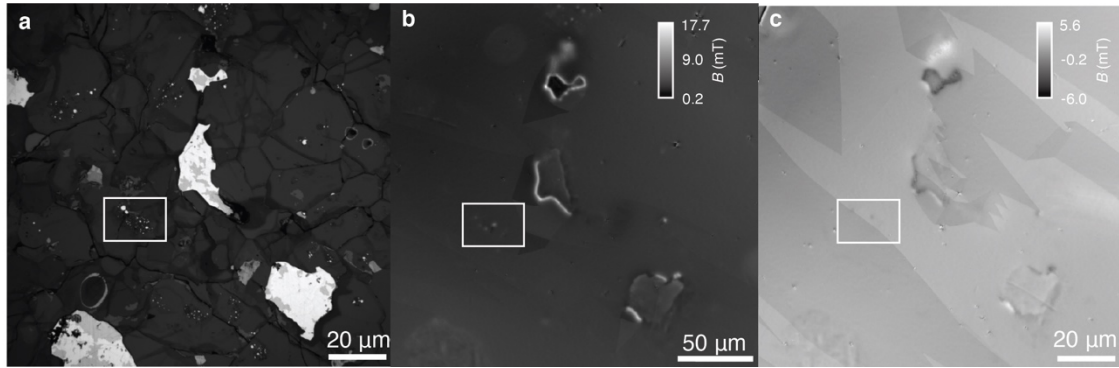


Figure S5. MOI images of Acapulco 30- μm thin section USNM 5967-1. **a)** Reflected light image. Bright grains are metal grains and dark grains are silicates (olivine and pyroxene). **b)** MOI image taken after application of a 1 T IRM. Brightness is seen along the rims of some of the metal grains, which we interpret as tetrataenite. Note that scale bar is field intensity relative to the non-magnetic background. **c)** MOI image after an IRM backfield application of 300 mT. The signal has mostly disappeared, indicating that the coercivity of remanence of the rims are generally <300 mT. Note that scale bar is field intensity relative to the non-magnetic background.

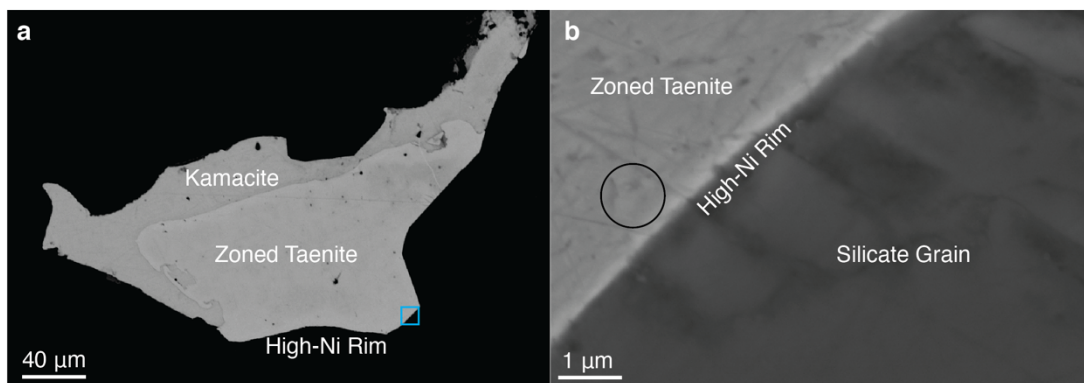


Figure S6. Electron microscopy images of metal grain with MOI fluorescence. **a)** BSE image of the center grain in Fig. S5, rotated 90 degrees counterclockwise. The areas of the rim with MOI fluorescence in Fig. S5 occur only where the zoned taenite is located in the grain. The rim of the zoned taenite region is enriched in Ni. **b)** Zoomed in secondary electron image of the blue-boxed region in (a). There bright, Ni-rich rim is evident, and is only about 200 nm wide. The black circle shows the location of an EDS spot measurement, which reported a composition of 42 wt.% Ni.

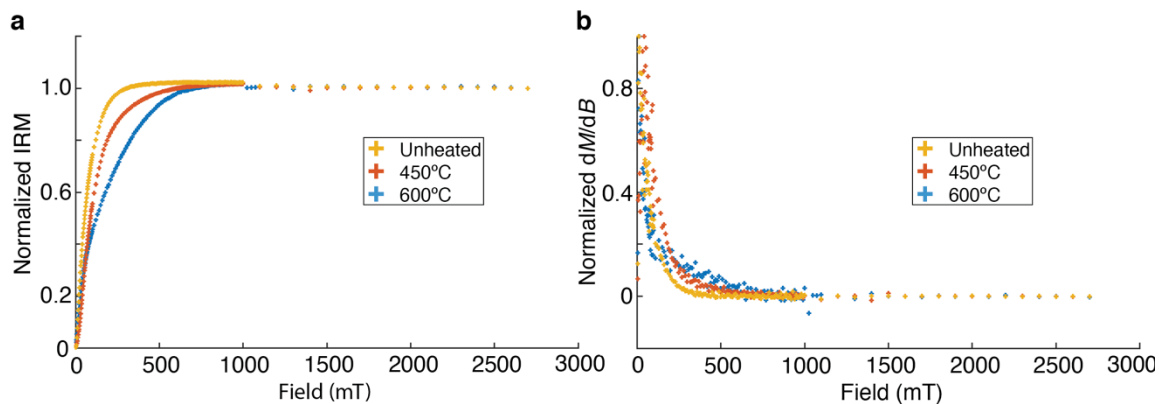


Figure S7. IRM acquisition on bulk sample NMMAC7 (interior). **a)** Normalized IRM versus field for NMMAC7 prior to heating (blue), after heating to 400°C (red), and after heating to 600°C (yellow). **b)** Normalized dM/dB versus field for NMMAC7 prior to heating (blue), after heating to 400°C (red), and after heating to 600°C (yellow).

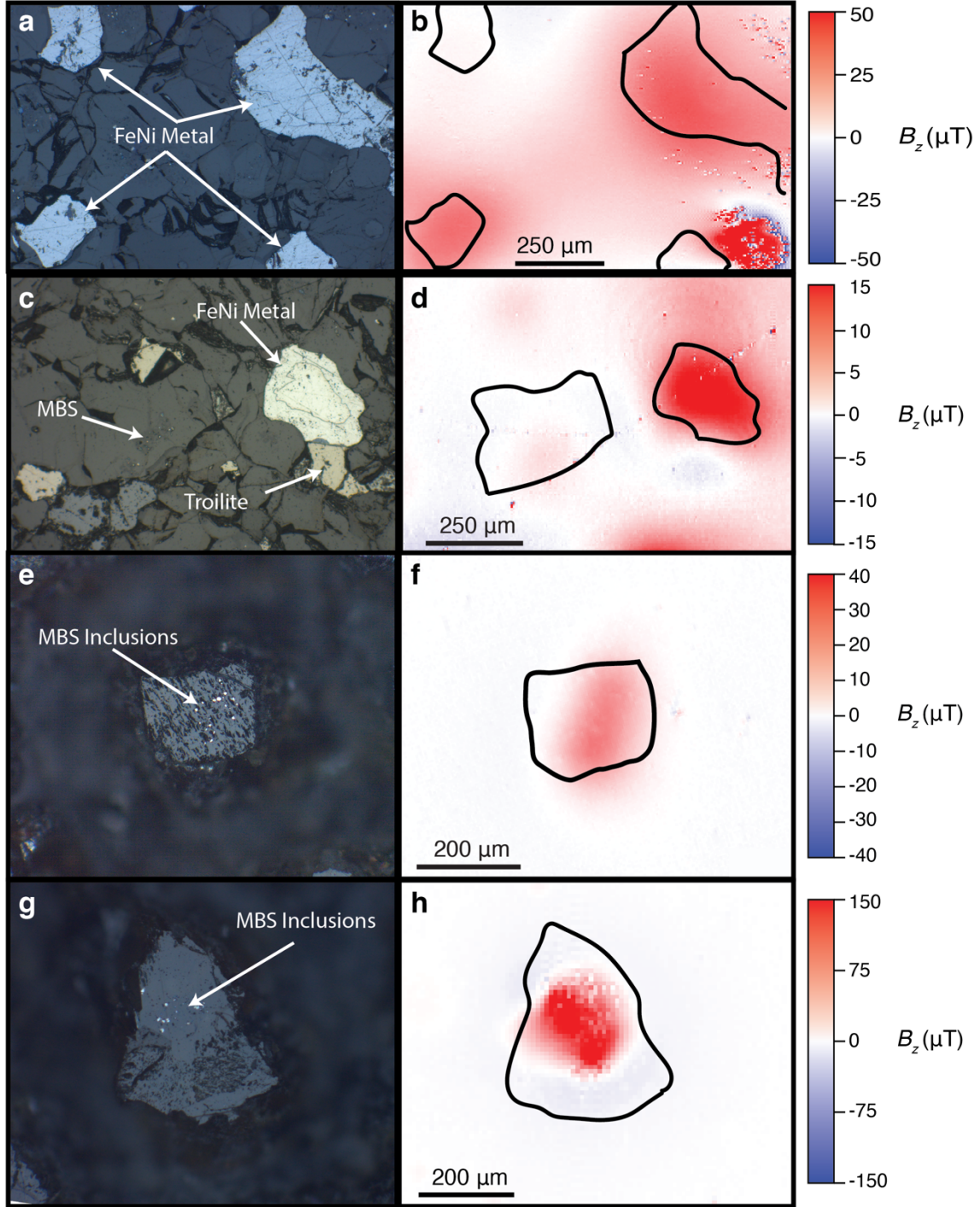


Figure S8. QDM maps of Acapulco after IRM application. **a, c)** Reflected light images of Acapulco 30-μm thin section USNM 5967-1. A diversity of metal and sulfide grains is seen in the images, including large interstitial FeNi grains, troilite, and an MBS. **b, d)** QDM maps of the vertical component of the magnetic field, B_z , of the thin section regions in (a, c) that was subjected to a 500 mT IRM. The maps were taken 120 μm above the sample. The fields-of-view are the same as in (a, c). The strongest magnetization comes from the largest FeNi

metal grains while a much weaker signal originates from the adjacent MBS in b). **e, g)** Reflected light images of MBSs isolated from the surrounding grains after milling a trough $\sim 300\ \mu\text{m}$ wide around them. There are scattered FeNi grains in the center of the MBSs. **f, h)** QDM maps of the vertical component of the magnetic field, B_z , of the MBSs in (e, g) that were subjected to a 1 T IRM. The maps were taken $5\ \mu\text{m}$ above the samples. The fields of view are the same as in (e, g), with the outline of the MBS denoted by black line. The magnetization of the MBS is collocated with the metal inclusions.

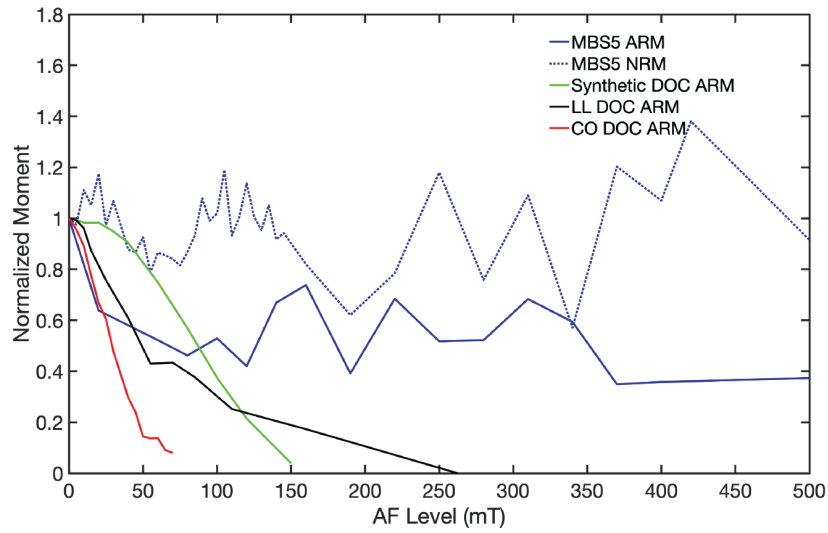


Figure S9. AF demagnetization of ARM in MBSs. AF demagnetization of a 200 μT bias field ARM for MBS 5 (130 mT AC field; solid line). The AF demagnetizations of 400 μT (150 mT AC field), 100 μT (290 mT AC field), and 200 μT (260 mT AC field) bias field ARMs are also shown for a synthetic DOC (Lappe et al., 2013), type 3.00 LL DOC (Fu et al., 2014), and type 3.00 CO DOC (Borlina et al., 2021), respectively, as a comparison. The NRM demagnetization of MBS5 is shown by the dashed line. Unlike the DOCs, the MBS shows inconsistent AF demagnetization above ~ 125 mT.

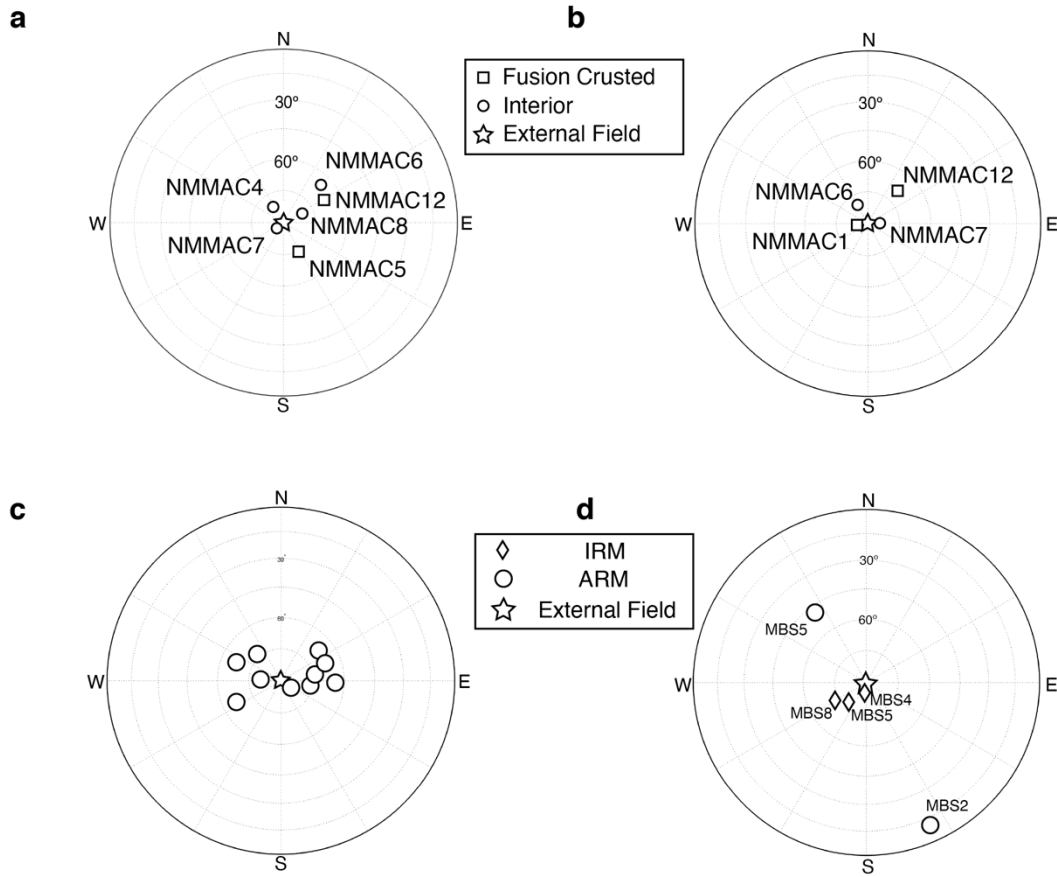


Figure S10. Repeated ARM and IRM acquisition for bulk samples and MBSs. **a)** Equal area stereonet showing the direction of the acquired ARM for interior (circles) and fusion-crusted (squares) bulk samples compared to the ARM bias field direction (star). **b)** Equal area stereonet showing the direction of the acquired IRM for interior (circles) and fusion-crusted (squares) bulk samples compared to the IRM bias field direction (star). **c)** Repeated ARM applications for interior bulks sample NMMAC 4 are shown by the green triangles. **d)** Equal area showing the direction of ARM (circle) and IRM (diamond) acquisition for MBSs compared to the direction of the bias field (star). MBS2 did not acquire an appreciable moment in the bias field direction while MBS5 exhibited limited acquisition in the field direction.

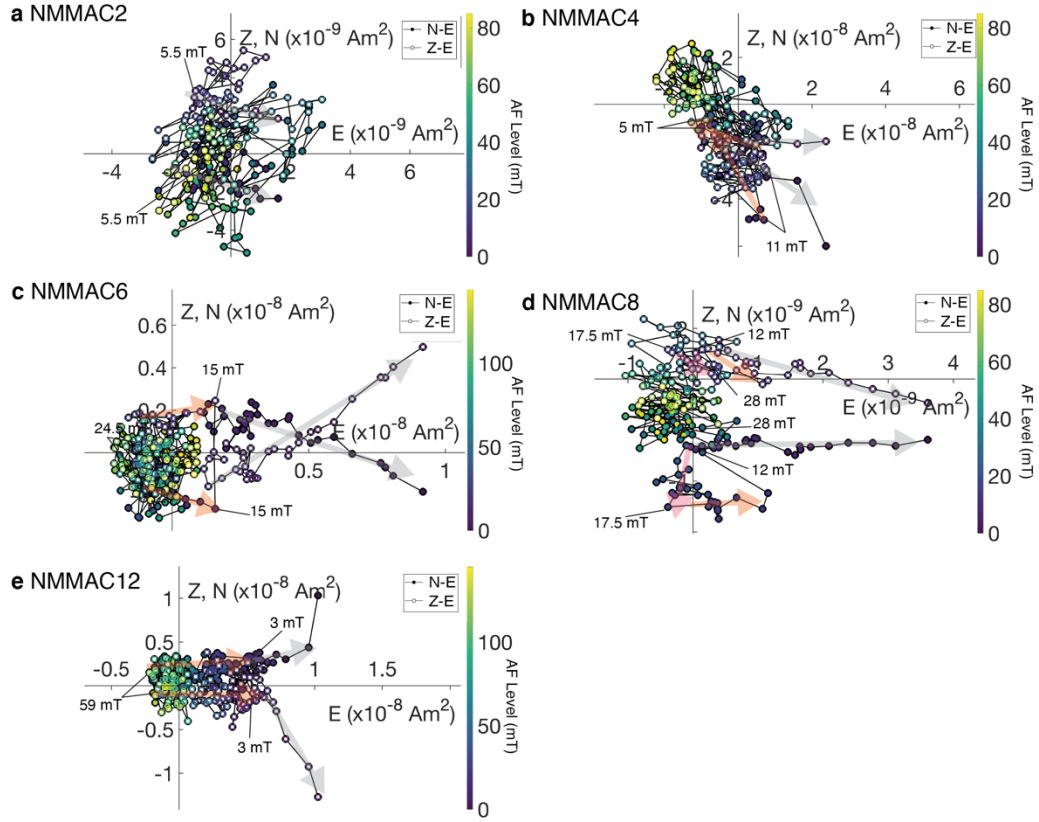


Figure S11. AF demagnetization of Acapulco bulk samples not shown in main text. **a)** Interior sample NMMAC2. **b)** Interior sample NMMAC4. **c)** Interior sample NMMAC6. **d)** Interior sample NMMAC8. **e)** Fusion-crust sample NMMAC12. Shown are orthographic projections of the NRM vectors during demagnetization. Closed symbols represent the north-east (N-E) projection and open symbols represent the up-east (Z-E) projection of the moment. The color bars to the right of each panel shows the AF levels. Grey arrows show the directions of the LCi/LCf component for each projection; orange arrows show the directions of the MCi/MCf component for each projection; Pink arrows show the directions of the additional MCi component in NMMAC 8.

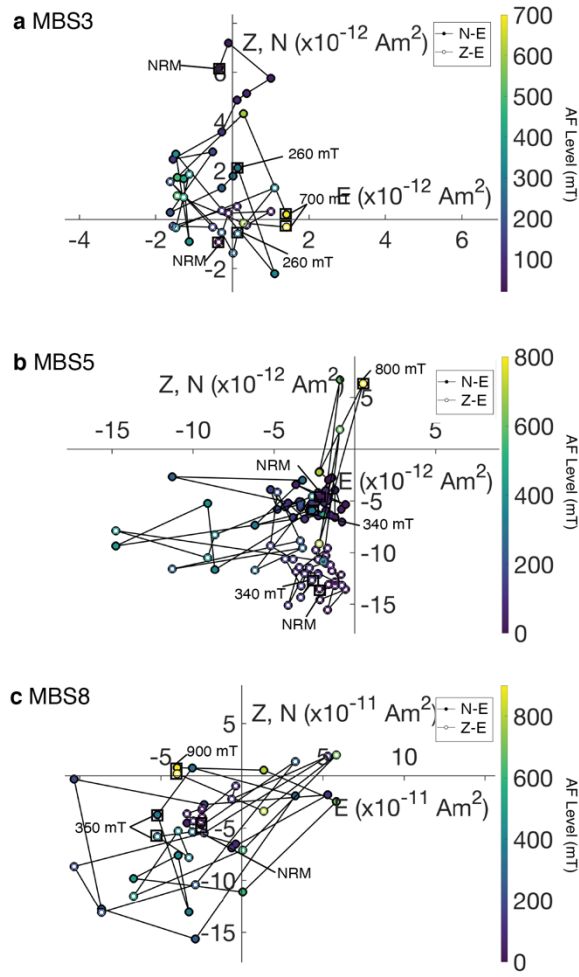


Figure S12. AF demagnetization of Acapulco MBSs. **a)** MBS3. **b)** MBS5. **c)** MBS8. Shown are orthographic projections of the NRM vectors during demagnetization. Closed symbols represent the north-east (N-E) projection and open symbols represent the down-east (Z-E) projection of the moment. The color bars to the right of each panel shows the AF levels. Grey arrows show the directions of the LC component for each projection; green arrows show the directions of the HC component for each projection.

Table S1. Rock magnetic properties of bulk samples

| Sample | Fusion Crusted? | Mass (mg) | NRM (Am^2) | 1 T IRM (Am^2) | NRM/mass (Am^2/kg) | A^p/A^0 | ARM ($^\circ$) | IRM ($^\circ$) |
|---------|-----------------|-----------|-----------------------|---------------------------|--------------------------------------|-----------|------------------|------------------|
| NMMAC1 | Yes | 31.5 | $2.68 \cdot 10^{-8}$ | $3.41 \cdot 10^{-6}$ | $8.51 \cdot 10^{-10}$ | - | - | 4.5 |
| NMMAC2 | No | 21.7 | $3.37 \cdot 10^{-9}$ | - | $1.55 \cdot 10^{-10}$ | - | - | - |
| NMMAC3 | No | 21.7 | $1.38 \cdot 10^{-8}$ | - | $6.36 \cdot 10^{-10}$ | - | - | - |
| NMMAC4 | No | 47.5 | $6.63 \cdot 10^{-9}$ | - | $1.40 \cdot 10^{-10}$ | 1.7 | 9.0 | - |
| NMMAC5 | Yes | 15.0 | $9.10 \cdot 10^{-8}$ | - | $6.07 \cdot 10^{-9}$ | 6.4 | 15.2 | - |
| NMMAC6 | No | 18.4 | $1.06 \cdot 10^{-8}$ | $1.24 \cdot 10^{-6}$ | $5.67 \cdot 10^{-10}$ | 2.5 | 25.6 | 10.3 |
| NMMAC7 | No | 24.1 | $1.97 \cdot 10^{-8}$ | $1.98 \cdot 10^{-6}$ | $8.17 \cdot 10^{-10}$ | 4.7 | 4.0 | 5.2 |
| NMMAC8 | No | 22.5 | $4.42 \cdot 10^{-9}$ | - | $1.96 \cdot 10^{-10}$ | 8.6 | 10.2 | - |
| NMMAC12 | Yes | 5.78 | $1.93 \cdot 10^{-8}$ | $2.12 \cdot 10^{-6}$ | $3.34 \cdot 10^{-9}$ | 10.7 | 21.7 | 21.3 |

Notes: The first column indicates the sample name. The second column denotes whether the sample is fusion-crusted and the third column provides each sample's mass. The fourth and fifth columns indicate the NRM and IRM of the samples. The sixth column provides the NRM per unit mass. The seventh column provides the moment after ARM application (A^p) divided by the moment prior to ARM application after full NRM demagnetization (A^0). The last two columns indicate the angles between the ARM- and IRM-gained and the ARM and IRM field application directions (θ_{ARM} and θ_{IRM}), respectively.

Table S2. Rock magnetic properties of MBSs

| Sample | NRM (Am^2) | 1 T IRM (Am^2) | A^p/A^0 | IRM ($^\circ$) |
|--------|-----------------------|---------------------------|-----------|------------------|
| MBS2 | $7.71 \cdot 10^{-12}$ | $3.22 \cdot 10^{-10}$ | 2.1 | - |
| MBS3 | $6.24 \cdot 10^{-12}$ | - | - | - |
| MBS4 | $3.70 \cdot 10^{-12}$ | $1.52 \cdot 10^{-9}$ | - | 3.4 |
| MBS5 | $1.39 \cdot 10^{-11}$ | $1.37 \cdot 10^{-9}$ | 1.5 | 12.9 |
| MBS8 | $6.89 \cdot 10^{-11}$ | $2.88 \cdot 10^{-9}$ | -- | 17.2 |
| MBS9 | $5.02 \cdot 10^{-12}$ | - | 2.6 | - |

Notes: The first column indicates the sample name. The second and third columns indicate the NRM magnetization and IRM magnetization of the samples. The fourth column provides the moment after ARM application (A^p) divided by the moment prior to ARM application after full NRM demagnetization (A^0). The last column indicates the angle between the IRM gained and the IRM field application directions (θ_{IRM}).

Table S3. Summary of PCA for the Acapulco bulk samples

| Sample | Strike/ Dip (°) | Component | AF Range (mT) | N | Inc (°) | Dec (°) | MAD (°) | DANG (°) | Origin- trending? | Paleointensity (μ T) |
|---------|--------------------|-----------|------------------|----|------------|------------|------------|-------------|----------------------|------------------------------|
| NMMAC1 | 0/90 | LCf | 0 – 4.5 | 8 | 36.5 | 78.6 | 12.4 | 44.4 | N | 82.1 \pm 15.7 |
| | | MCf | 5.5 – 29.0 | 44 | -20.8 | 345.8 | 44.8 | 36.1 | Y | 8.7 \pm 3.8 |
| NMMAC2 | 0/90 | LCi | 0 – 5.5 | 10 | 17.7 | 109.2 | 20 | 98.7 | N | 44.7 \pm 11.2 |
| NMMAC3 | 0/90 | LCi | 0 – 10 | 18 | 28.1 | 158.8 | 30.5 | 131.6 | N | 45.5 \pm 17.3 |
| | | MCI | 11 – 24.5 | 28 | -45 | 5.5 | 13.8 | 30.2 | N | 123.8 \pm 51.2 |
| NMMAC4 | 0/90 | LCi | 0 – 5 | 9 | 1.2 | 144.1 | 14.5 | 40.4 | N | -- |
| | | MCI | 5.5 – 10.0 | 12 | -14.5 | 348.3 | 15.4 | 147.7 | N | -- |
| NMMAC5 | 180/90 | LCf | 0 – 14.0 | 26 | -3 | 55.5 | 9.1 | 12.5 | N | -- |
| | | MCf | 14.5 – 66.0 | 63 | 6.7 | 81.5 | 41.7 | 24.8 | Y | -- |
| NMMAC6 | 0/90 | LCi | 0 – 15.0 | 29 | -37.4 | 115 | 12.3 | 47.8 | N | -- |
| | | MCI | 17.5 – 24.5 | 15 | -21.3 | 135.2 | 33 | 29.4 | Y | -- |
| NMMAC7 | 180/90 | LCi | 0 – 13.0 | 25 | -11.8 | 69.5 | 22.9 | 42.8 | N | 35.9 \pm 9.3 |
| NMMAC8 | 0/90 | LCi | 0 – 12.0 | 23 | 28.7 | 89 | 14.3 | 73.3 | N | 42.6 \pm 4.2 |
| | | MC1i | 12.5 – 17.5 | 11 | 40.7 | 74.2 | 29.3 | 100.4 | N | -3.8 \pm 17.3 |
| | | MC2i | 18.0 – 28.0 | 18 | 24.9 | 192.4 | 31.3 | 39.5 | N | 89.8 \pm 22.5 |
| NMMAC12 | 180/90 | LCf | 0 – 3.0 | 5 | 54.9 | 30.3 | 15.5 | 29.2 | N | 79.9 \pm 20.3 |
| | | MCf | 3.5 – 59.0 | 78 | 12.6 | 88.2 | 46.2 | 27.6 | Y | 6.6 \pm 2.3 |

Notes: The first column denotes the sample name and the second column lists the orientation of how the sample was measured (core plate strike and dip). The third column provides the component name (LCf/LCi and MCf/MCI) and the fourth column details AF range the component was unblocked over. The fifth column details the number of points used in the PCA fit. The sixth through eight columns provide the inclination, declination, and maximum angular deviation respectively for each component. The ninth column lists the deviation angle for each fit. The tenth column lists whether an unanchored fit to the component over the given AF range was origin-trending. The final column lists the paleointensities calculated via the IRM method (see main text methods and materials section).

Data Set S1. *Text file for FORC data taken on unheated bulk interior sample NMMAC 7.*

Data Set S2. *Text file for FORC data taken on bulk interior sample NMMAC 6 after heating to 600°C for 20 minutes.*

References

- Bland, P., Zolensky, M., Benedix, G., & Sephton, M. (2006). Weathering of chondritic meteorites. *Meteorites and the Early Solar System II*, 1, 853-867.
- Boland, J. N., & Duba, A. (1981). Solid-state reduction of iron in olivine-planetary and meteoritic evolution. *Nature*, 294(5837), 142-144.
- Borlina, C. S., Weiss, B. P., Bryson, J. F. J., Bai, X., Lima, E. A., Chatterjee, N., & Mansbach, E. N. (2021). Paleomagnetic evidence for a disk substructure in the early solar system. *Science Advances*, 7(42), eabj6928.
- Dos Santos, E., Gattacceca, J., Rochette, P., Fillion, G., & Scorzelli, R. B. (2015). Kinetics of tetraenaite disordering. *Journal of Magnetism and Magnetic Materials*, 375, 234-241.
- Dunlop, D., & Özdemir, Ö. (1997). *Rock magnetism: Fundamentals and Frontiers* (1 ed.): Cambridge University Press.
- Dunlop, D. J., & Argyle, K. S. (1997). Thermoremanence, anhysteretic remanence and susceptibility of submicron magnetites: Nonlinear field dependence and variation with grain size. *Journal of Geophysical Research: Solid Earth*, 102(B9), 20199-20210.
- Einsle, J. F., Eggeman, A. S., Martineau, B. H., Saghi, Z., Collins, S. M., Blukis, R., et al. (2018). Nanomagnetic properties of the meteorite cloudy zone. *Proceedings of the National Academy of Sciences*, 115(49), E11436-E11445.
- El Goresy, A., Zinner, E., Pellas, P., & Caillet, C. (2005). A menagerie of graphite morphologies in the acapulco meteorite with diverse carbon and nitrogen isotopic signatures: Implications for the evolution history of acapulcoite meteorites. *Geochimica et Cosmochimica Acta*, 69(18), 4535-4556.
- Fu, R. R., Lima, E. A., Volk, M. W. R., & Trubko, R. (2020). High-sensitivity moment magnetometry with the quantum diamond microscope. *Geochemistry, Geophysics, Geosystems*, 21(8), e2020GC009147.
- Fu, R. R., Weiss, B. P., Lima, E. A., Harrison, R. J., Bai, X.-N., Desch, S. J., et al. (2014). Solar nebula magnetic fields recorded in the Semarkona meteorite. *Science*, 346(6213), 1089-1092.
- Gattacceca, J., Suavet, C., Rochette, P., Weiss, B. P., Winklhofer, M., Uehara, M., & Friedrich, J. M. (2014). Metal phases in ordinary chondrites: Magnetic hysteresis properties and implications for thermal history. *Meteoritics & Planetary Science*, 49(4), 652-676.
- Glenn, D. R., Fu, R. R., Kehayias, P., Sage, D. L., Lima, E. A., Weiss, B. P., & Walsworth, R. L. (2017). Micrometer-scale magnetic imaging of geological samples using a quantum diamond microscope. *Geochemistry, Geophysics, Geosystems*, 18(8), 3254-3267.
- Harrison, R. J., & Feinberg, J. M. (2008). Forcinel: An improved algorithm for calculating first-order reversal curve distributions using locally weighted regression smoothing. *Geochemistry, Geophysics, Geosystems*, 9(5).
- Kirschvink, J. L. (1980). The least-squares line and plane and the analysis of palaeomagnetic data. *Geophysical Journal International*, 62(3), 699-718.

- Lappe, S. L. L., Feinberg, J. M., Muxworthy, A. R., & Harrison, R. J. (2013). Comparison and calibration of nonheating paleointensity methods: A case study using dusty olivine. *Geochemistry, Geophysics, Geosystems*, 14(7), 2143-2158.
- Leroux, H., Libourel, G., Lemelle, L., & Guyot, F. (2003). Experimental study and REM characterization of dusty olivines in chondrites: Evidence for formation by in situ reduction. *Meteoritics & Planetary Science*, 38(1), 81-94.
- McCoy, T. J., Corrigan, C. M., Dickinson, T. L., Benedix, G. K., Schrader, D. L., & Davidson, J. (2019). Grove Mountains (GRV) 020043: Insights into acapulcoite-lodranite genesis from the most primitive member. *Geochemistry*, 79(4), 125536.
- Palme, H., Schultz, L., Spettel, B., Weber, H. W., Wänke, H., Michel-Levy, M. C., & Lorin, J. C. (1981). The Acapulco meteorite: Chemistry, mineralogy and irradiation effects. *Geochimica et Cosmochimica Acta*, 45(5), 727-752.
- Tauxe, L. (2010). *Essentials of Paleomagnetism*: University of California Press.
- Uehara, M., Beek, C. J., Gattacceca, J., Skidanov, V. A., & Quesnel, Y. (2010). Advances in magneto-optical imaging applied to rock magnetism and paleomagnetism. *Geochemistry, Geophysics, Geosystems*, 11(5).
- Uehara, M., Gattacceca, J., Leroux, H., Jacob, D., & van der Beek, C. J. (2011). Magnetic microstructures of metal grains in equilibrated ordinary chondrites and implications for paleomagnetism of meteorites. *Earth and Planetary Science Letters*, 306(3), 241-252.
- Wang, H., Wang, J., Chen-Wiegart, Y. C., & Kent, D. V. (2015). Quantified abundance of magnetofossils at the Paleocene-Eocene boundary from synchrotron-based transmission X-ray microscopy. *Proceedings of the National Academy of Sciences*, 112(41), 12598-12603.
- Werwiński, M., & Marciniak, W. (2017). Ab initio study of magnetocrystalline anisotropy, magnetostriction, and fermi surface of $L1_0\text{FeNi}$ (tetraenaite). *Journal of Physics D: Applied Physics*, 50(49).
- Williams, G. M., & Pavlovic, A. S. (1968). The magnetostriction behavior of iron single crystals. *Journal of Applied Physics*, 39(2), 571-572.
- Zipfel, J., Palme, H., Kennedy, A. K., & Hutcheon, I. D. (1995). Chemical composition and origin of the Acapulco meteorite. *Geochimica et Cosmochimica Acta*, 59(17), 3607-3627.